

Chapter 5

Oxidation of Alloys I: Single Phase Scales

5.1 INTRODUCTION

Most metallic materials of practical importance are alloys. Even mild steel invariably contains some level of carbon and usually small amounts of other elements. The alloys and coatings employed for heat-resisting applications are usually based on iron, nickel or cobalt and contain chromium and/or aluminium to provide protective oxide scales.

The choice of chromium and aluminium is based on the slow rate at which their oxides grow (Table 1.1) and the fact that these oxides are considerably more stable than those of iron, nickel or cobalt (Table 2.1). Thus Cr_2O_3 and Al_2O_3 are thermodynamically favoured and will form preferentially if this is kinetically possible. Alloy additions of silicon would seem to meet the same criteria and possess the added advantage of being readily available in the economic form of ferrosilicon. However, the use of silicon as an alloying additive is limited by metallurgical constraints. Since silicon decreases the weldability and toughness (or impact resistance) of steels and nickel-base alloys, its concentration is limited to such low levels that formation of a silica layer alone cannot be achieved. However, silica scales play a protective role in the high-temperature performance of a number of nonoxide ceramics, eg, MoSi_2 , SiC and Si_3N_4 .

A very large research and development effort has led to the production of present day heat-resisting materials and is continuing in the search for better ones. The literature in this field is consequently vast, and no attempt will be made to review it here. Instead the focus will be on developing an understanding of the different modes of alloy oxidation, finding ways of predicting the circumstances under which each of these modes operates, and calculating the rate of alloy consumption in each case.

This chapter is concerned principally with the factors which determine whether an alloy forms a protective scale of the desired low diffusivity oxide (usually Cr_2O_3 or Al_2O_3) or some other reaction products. The number of possible outcomes is large and increases with alloy complexity, each additional alloy component providing an additional degree of thermodynamic

freedom, as seen in Eq. [2.35]. Even a simple binary alloy can develop two-phase regions within the scale and/or form nonplanar interfaces between adjacent phases. It can also precipitate oxide of its more reactive component inside the alloy in the process of internal oxidation.

Alloy components will form oxides of different stabilities. Moreover, the component metals will generally have differing mobilities in each relevant phase, alloy and oxides, as well as varying intersolubilities. The situation can be further complicated by the existence of multiple phases within the alloy (eg, ferrite + Fe_3C in steel; $\gamma + \gamma'$ in superalloys; etc.), the formation of ternary product phases and occasionally the development of low melting eutectics such as $\text{FeO}-\text{Fe}_2\text{SiO}_4$ on silicon steels. In addition the distribution of reaction product phases, that is to say the reaction morphology, will usually change with time. In an initial, transient stage, all reactive alloy components oxidise, yielding a product with essentially the same relative proportions of metallic constituents as the parent alloy. Subsequently, local equilibrium is achieved at alloy-scale and scale-gas interfaces, and steady-state reaction follows. During this stage, the scale morphology and composition are invariant with time, and the phase diagram ‘diffusion path’ description applies. Heat-resisting alloy design is directed towards achieving a slow growing oxide scale during the steady state. Ultimately, the alloy component responsible for protective oxide formation is exhausted or ceases to be available, and a final breakdown stage ensues. Eventually, of course, the final oxidation product contains reactive alloy components in the same proportions as did the original alloy.

We consider first some experimental results for alloy oxidation selected to illustrate the diversity of reaction product morphologies. Attention is then concentrated on the situation in which a single-phase oxide is the only reaction product. Its possible morphologies, growth rates and protective value are then investigated, drawing heavily on the extensive theoretical treatments developed by Wagner and added to by others. Finally, some consideration is given to predicting the lifetime of an alloy component forming a protective scale in the steady-state regime.

For detailed descriptions of the oxidation behaviour of individual alloys, the reader is referred to the proceedings of the many conferences addressing the topic. Some have been established as regular international conference proceedings [1–3]. In addition, a useful summary of commercial alloy performance in various high-temperature environments has been provided by Lai [4].

5.2 SELECTED EXPERIMENTAL RESULTS

Many high-temperature alloys are designed to form protective chromia (Cr_2O_3) scales. Examples include stainless and heat-resisting steels and nickel base alloys such as Incolloys and some Inconels. Compositions of some alloys are given in [Table 5.1](#), with more in Appendix A.

TABLE 5.1 Nominal Compositions of Some Heat Resisting Alloys (wt%)

Alloy	Fe	Ni	Cr	Si	Mn	C	Other
P91	bal	0.3	9	0.4	0.4	0.10	1Mo, 0.2 V
310	bal	20	25	1.5	2.0	0.25	
347	bal	11	18	1.0	2.0	0.08	Nb (8×%C)
253 MA	bal	11	21	1.7	0.8	0.08	0.08 Ce, 1Al
800	bal	31	21			0.07	0.25Al, 0.35Ti
HP (cast)	bal	35	25	1.8	0.2	0.44	0.8Nb
601	14	bal	23			0.06	1.4Al, 0.5Ti
214	3	bal	16	0.2	0.5	0.05	4.5Al, 0.01Y
Kanthal AF	bal		21				5.1Al, 0.08Ti, 0.06Zr
MA956	bal		20				4.5Al, 0.5Ti, 0.5Y ₂ O ₃

The range of possible steady-state behaviours of chromia-forming alloys is shown in Fig. 5.1. A model binary alloy of Fe-28 Cr (all compositions in wt.%) is seen in Fig. 5.1A to form an external scale of Cr₂O₃ alone when reacted with oxygen at 900°C. The scale grows slowly, with $k_p = 1.4 \times 10^{-9} \text{ cm}^2 \text{ s}^{-1}$, representing the desired outcome of single-phase protective layer growth. However, when the alloy chromium content is too low, this protective layer does not form. A model alloy of Fe-7.5 Cr reacted with oxygen at 850°C to form a fast growing, iron-rich scale, as shown in Fig. 5.1B. Dilute alloys can fail to form a protective scale even if the oxygen partial pressure is too low to oxidise any component except chromium. As seen in Fig. 6.1, Cr₂O₃ is internally precipitated within an Fe-5 Cr alloy reacted at 1000°C, in a low p_{O_2} atmosphere. Oxygen had dissolved in the alloy, diffusing inwards to react with solute chromium and precipitate its oxide. It is obviously desirable to be able to predict the minimum alloy chromium level required to form external, rather than internal, Cr₂O₃ and thereby protect the alloy iron base from oxidation.

Commercial chromia-forming alloys can be even more complex in their reaction morphologies. Oxidation of Inconel 601, which contains a low level of aluminium in addition to 23% Cr (Table 5.1), is seen in Fig. 5.1C to form an external Cr₂O₃ scale and internal Al₂O₃ precipitates. A cast heat-resisting steel (HP grade, 25Cr-35Ni) was oxidised in steam at 1000°C to form a two-layered scale (Fig. 5.1D). A continuous chromia inner layer formed, but a manganese-rich spinel (MCr₂O₄ with M a mixture of Mn, Fe and Ni) layer grew on top. Clearly it is necessary to establish the conditions under which the desired oxide scale can prevent the oxidation of other alloy components. In the

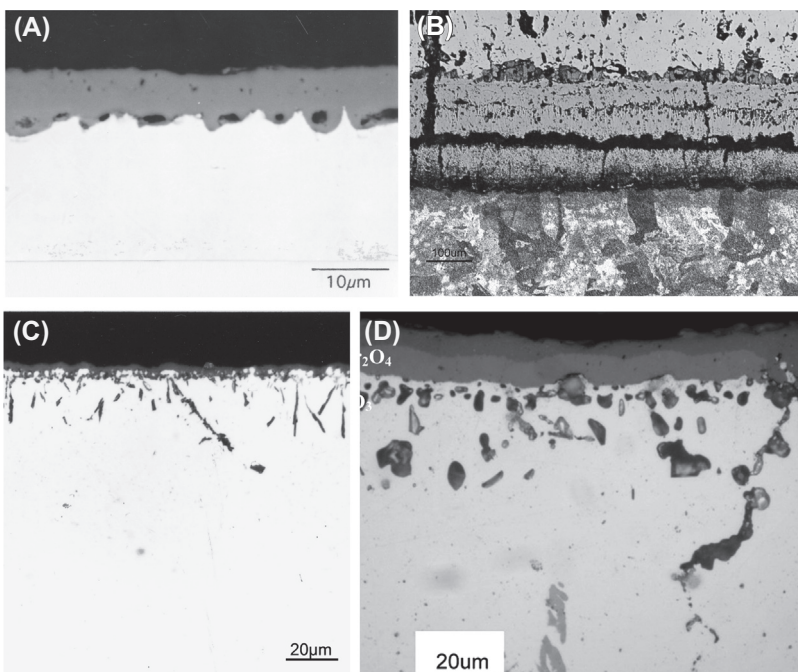


FIGURE 5.1 (A) External Cr_2O_3 scale grown on Fe-28Cr at $T = 1000^\circ\text{C}$; (B) iron-rich scale grown on Fe-7.5Cr at $T = 850^\circ\text{C}$ in pure O_2 ; (C) simultaneous external Cr_2O_3 scale growth and internal Al_2O_3 precipitation, alloy IN 601 at $T = 1000^\circ\text{C}$; and (D) two-layered scale of spinel and Cr_2O_3 together with internal attack on HP35 cast, heat-resisting steel oxidised in steam at 1000°C .

example of Fig. 5.1D, the chromia layer had allowed outward diffusion of manganese to form a surface layer of spinel. The chromia scale shown in Fig. 5.1C had allowed oxygen to diffuse into the alloy, precipitating alumina. In these particular cases, the chromia scale nonetheless protected the alloy iron and nickel from reaction.

Alloy oxidation can also lead to changes within the alloy itself. We have already encountered the example of internal oxidation, which reflects the inward diffusion of an oxidant. Microstructural changes in the alloy can also result from outward diffusion of alloy components. A common example is decarburisation. Fig. 5.2 shows a cross-section of a tube wall from a failed boiler superheater unit. The overheating of this tube led to rapid oxidation, tube wall thinning and subsequent mechanical failure as the steam pressure inside the tube ruptured its wall. The tube metal was a $1\frac{1}{4}\text{Cr}-1\text{Mo}$ steel, which has a microstructure of ferrite plus pearlite. The pearlite (a mixture of lamellar Fe_3C and ferrite) is seen in the lower part of the wall cross-section to have coarsened and spheroidised. In the upper part of the cross-section, near the rapidly oxidising external surface, the carbide has almost completely

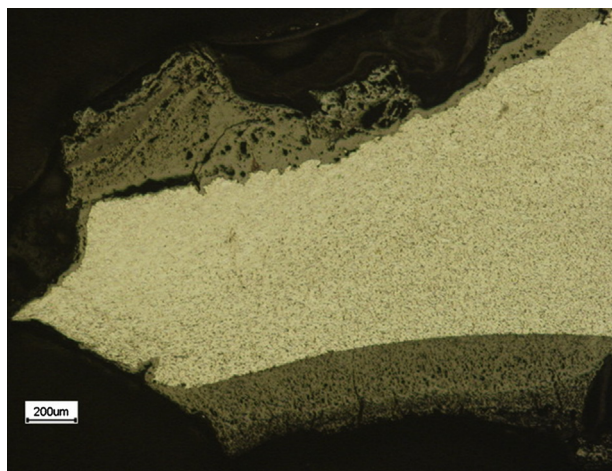
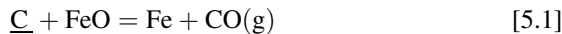


FIGURE 5.2 Cross-section of tube wall ($1\frac{1}{4}$ Cr + 1Mo steel) from failed boiler superheater unit, showing decarburisation beneath the outer (upper) surface.

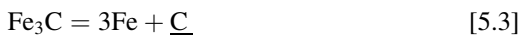
disappeared. Here the solute carbon from within the ferrite was oxidised at the steel-scale interface via the reaction:



for which

$$\Delta G_1^\circ = 147,760 - 150.1T \text{ J mol}^{-1} \quad [5.2]$$

The resulting CO(g) escaped through the porous scale. As a result, the carbon activity in the steel at the surface was lowered, causing the cementite to dissolve:



Solute carbon diffused from the interior carbide dissolution front to the steel-scale interface, there to be oxidised and removed.

Selective oxidation of an alloy constituent lowers its concentration within the alloy. If alloy diffusion is rapid compared with the scaling rate, then the change in alloy concentration is averaged over a large region, and the concentration change at the alloy-scale interface will be small. However, if alloy diffusion is relatively slow, replenishment of the selectively removed metal is hindered, and the concentration of that element is depleted in the subsurface zone, as illustrated schematically in Fig. 5.3. When the concentration of one component is decreased, the concentrations of others are increased. The extent to which they are enriched is governed by the rates at which they diffuse away from the surface into the alloy interior. These changes in subsurface composition can cause alterations in the phase constitution of this region. A simple

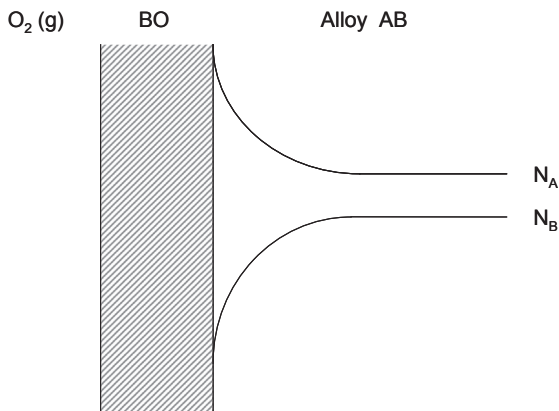


FIGURE 5.3 Depletion of selectively oxidised alloy component and enrichment of nonoxidised component in binary alloy.

example of practical importance is the precipitation of a copper-rich phase at the surface of steel during hot working [5].

A significant quantity of steel is produced by remelting scrap. Most scrap impurities are removed during the steelmaking process, but some, such as copper and tin, remain. Several successive cycles of steelmaking and recycling as scrap lead to an increase in the concentration of ‘residuals’ such as copper to levels far above those found in steel produced from iron ore. Oxidation of steel is inevitable during hot working (reheating, rolling, etc.), producing a scale of iron oxide, but leaving the copper unreacted. The resulting increase in copper concentration in the steel beneath the scale can exceed the solubility limit, precipitating a copper-rich Cu-Fe phase. An example is shown in Fig. 5.4.

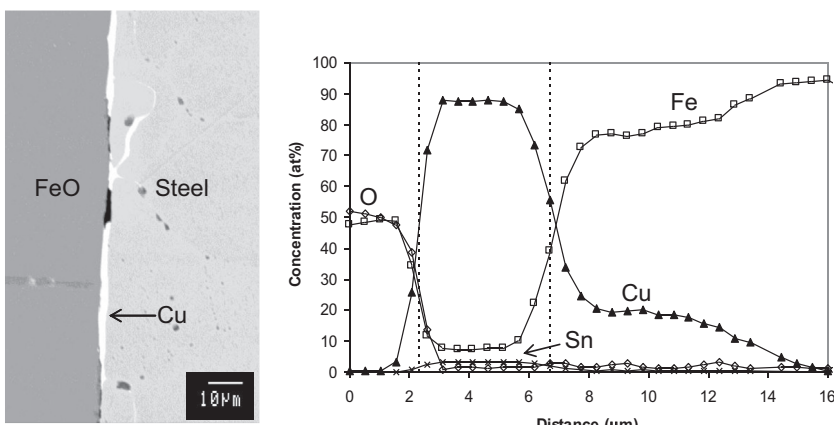


FIGURE 5.4 Copper enrichment beneath iron oxide scale grown on a 0.47Cu steel at $T = 1100^\circ\text{C}$. Left: SEM view of cross-section; right: EPMA scan.

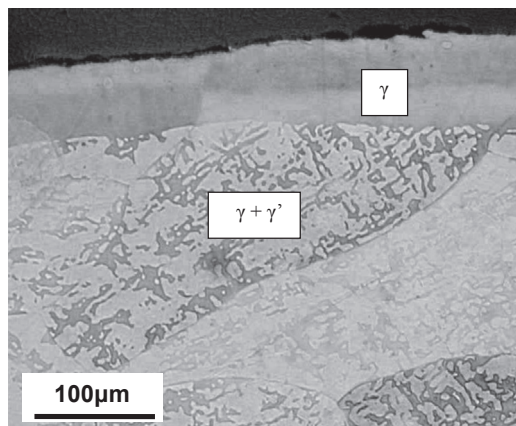


FIGURE 5.5 Dissolution of γ' - Ni_3Al in subsurface region of γ - γ' model alloy (Ni-23Al) due to selective aluminium oxidation at 1200°C .

If the temperature is above about 1100°C , this phase is liquid and penetrates the steel grain boundaries. Mechanical working of the steel in this state causes cracking, a phenomenon known as ‘hot shortness’.

The selective removal from an alloy of a metal by its preferential oxidation can drive other phase changes within the subsurface zone. An example is shown in Fig. 5.5, where selective oxidation of aluminium from a two-phase γ -Ni plus γ' - Ni_3Al alloy led to dissolution of the aluminium-rich γ' -phase, as aluminium diffused out of the subsurface zone. Selective oxidation of aluminium from β - NiAl does not at first cause a phase change, but it does lead to the development of cavities at the alloy-scale interface, as shown in Fig. 5.6.

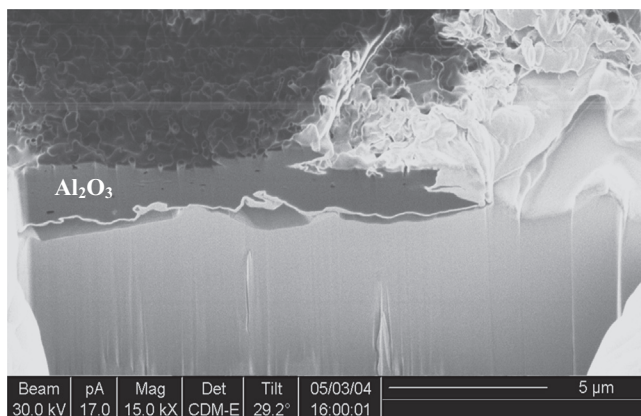


FIGURE 5.6 Cavity formation at β - NiAl surface due to selective aluminium oxidation at 1200°C .

Taking as a measure of success the ability of an alloy to form a single-phase scale of the desired oxide, it is desirable to be able to predict the conditions (alloy composition, p_{O_2} and temperature) under which this will be the result. As seen in this preliminary examination, it is necessary to predict not only when the desired oxide will form preferentially, but also when it forms as an external layer rather than an internal precipitate. Further, it is necessary to predict the effect of the external layer on the oxidation of other alloy components and on microstructural changes in the alloy subsurface region. We consider first the utility of phase diagrams in predicting diffusion paths and thereby reaction morphologies.

5.3 PHASE DIAGRAMS AND DIFFUSION PATHS

During the steady-state period of alloy oxidation, the scale morphology, ie, the identity and spatial arrangement of phases in the reacting system, is time invariant. This situation is conveniently represented by a diffusion path mapped onto the relevant phase diagram on the assumption that local equilibrium is in effect. The general nature of the problem is examined using the Ni-Cr-O isothermal section [6] shown in Fig. 5.7.

In this particular system, two simple oxides, NiO and Cr_2O_3 , and a ternary spinel, NiCr_2O_4 , can exist, and the degree of miscibility or intersolubility of the oxides is very limited. As seen from the diagram, all three oxides can

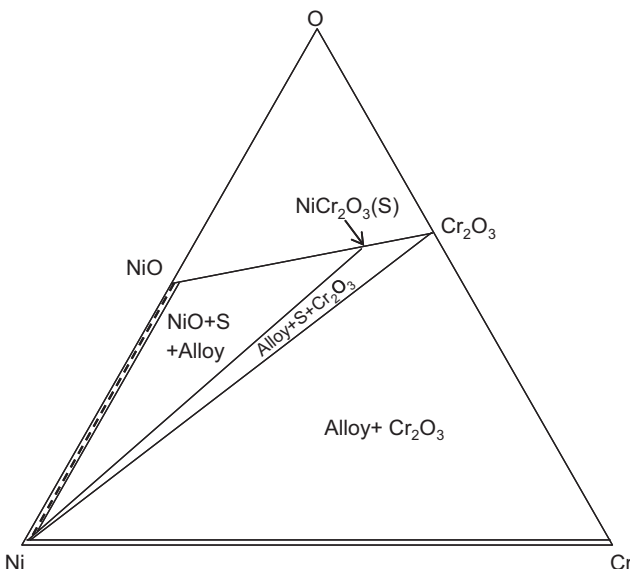


FIGURE 5.7 Isothermal section of Ni-Cr-O phase diagram at $T = 1000^\circ\text{C}$ [6]. With kind permission from Springer Science and Business Media.

coexist at equilibrium with $p_{O_2} = 1 \text{ atm}$, as can two-phase mixtures of $\text{NiO} + \text{NiCr}_2\text{O}_4$ and $\text{NiCr}_2\text{O}_4 + \text{Cr}_2\text{O}_3$. Thus specifying the ambient conditions is insufficient to determine the oxide which will be stable at the surface of a growing scale. Obviously, at least the alloy composition is required as well.

Local equilibrium at the alloy-scale interface is specified by the tie-lines joining alloy composition points to the corresponding oxides. According to Fig. 5.7 then, all Ni-Cr alloys containing $N_{\text{Cr}} \geq 0.03$ should form the desired oxide Cr_2O_3 at 1000°C . However, experimental investigations of alloy reactions with pure oxygen and other oxidising gases [7–10] have shown that a minimum chromium level of 10–20% is required to ensure the selective formation of Cr_2O_3 . The major reason for the discrepancy is chromium depletion in the alloy subsurface zone. The chromium concentration at the alloy-scale interface is reduced (by its selective oxidation) to a value significantly lower than that of the bulk alloy. In order to relate the alloy chromium mole fraction value, N_{Cr} , to the interfacial value, $N_{\text{Cr},i}$, it is necessary to analyse the alloy diffusion process.

The same difficulty arises in the case of Fe-Cr alloy oxidation. An isothermal section of the Fe-Cr-O phase diagram is shown in Fig. 2.5. As discussed earlier, the minimum value of N_{Cr} necessary to thermodynamically stabilise Cr_2O_3 formation is about 0.04. Experimental observations [7,11], however, put the critical alloy concentration at about 14% at 1000°C . Again, a principal reason for the difference is a lowering of the value $N_{\text{Cr},i}$ as a result of relatively slow alloy diffusion. The Co-Cr system exhibits an even greater extent of depletion, requiring up to 30% chromium to provide the critical interfacial value, estimated as $N_{\text{crit}} \approx 0.01$, required for Cr_2O_3 formation.

The question of how to deal with the alloy depletion problem is addressed in the next section. Returning now to the different reaction morphologies shown in Fig. 5.1, we see that they are consistent with the phase diagram, once allowance is made for surface alloy depletion. Thus the Fe-28Cr has enough chromium to sustain $N_{\text{Cr},i} > N_{\text{Cr,crit}}$, and a Cr_2O_3 scale results. A small degree of depletion in the Fe-7.5Cr alloy is sufficient to lower $N_{\text{Cr},i}$ below the critical value, and the diffusion path shown in Fig. 5.8 results. It is noted that the Fe-28Cr alloy develops a convoluted alloy-scale interface, at which voids are nucleated. Neither effect is predictable from the phase diagram without detailed knowledge of the local diffusion processes.

Reaction morphologies depend on oxygen partial pressure as well as alloy composition. The internal precipitate morphology of Fig 6.1 was produced in a gas with p_{O_2} too low to oxidise iron, so that Cr_2O_3 was the only stable reaction product. The formation of internally precipitated Cr_2O_3 corresponds to the development of a two-phase region, as shown by the diffusion path in Fig. 5.8. For comparison, a diffusion path is shown for external (single-phase) Cr_2O_3 formation at a higher alloy N_{Cr} value. Both paths terminate at the same oxygen potential but at different μ_{Cr} and μ_{Fe} values. It is obviously not possible to

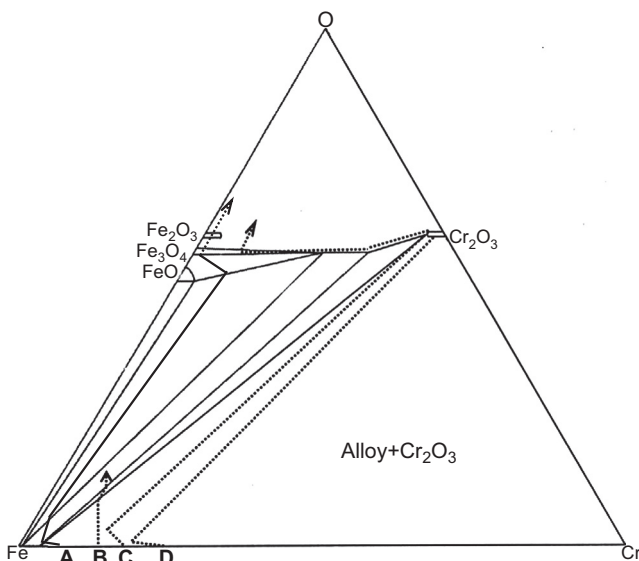


FIGURE 5.8 Diffusion paths on Fe-Cr-O phase diagram corresponding to (A) depletion and iron-rich oxide growth, (B) internal, (C) combined internal and external and (D) external chromium oxidation.

predict from the phase diagram alone which of the two morphologies will result for a particular alloy composition. Again, a diffusional analysis will be required.

As already mentioned, even when an external single-phase Cr_2O_3 layer forms in contact with the alloy surface, there remains the possibility of additional oxide formation. Formation of a spinel layer on top of the chromia, as illustrated in Fig. 5.1D, is a common result for heat-resisting steels. A schematic diffusion path for this type of scale morphology is shown for the Fe-Cr-O system in Fig. 5.8. Clearly the outer layer can develop only if the second metal is soluble in Cr_2O_3 and can diffuse through it at a sufficient rate. We return to this question in Chapter 7.

The complex reaction morphologies shown here are all consistent with steady-state local equilibrium having been established within the reacting systems. This was shown experimentally in each case by the observations that the morphologies were time invariant as the extent of reaction increased. It is also evident from the fact that the sequence of phase assemblages making up the morphology can, in each case, be represented by a diffusion path on the relevant phase diagram.

It is clear that phase diagrams of the type A-B-O can be used to describe the oxidation morphologies of binary alloys, AB. However, diffusion within

the alloy in general leads to surface concentrations which differ from those of the bulk alloy. In order to predict alloy oxidation behaviour, it is necessary to be able to calculate these concentration changes. We now consider the diffusion processes supporting growth of a single-phase scale on a binary alloy. In general, such an oxide can contain both alloy components, depending on the intersolubility of AO and BO, and their relative stabilities. We consider first the simplest case, where one alloy component remains completely unoxidised, and a pure binary oxide results from selective oxidation of the other.

5.4 SELECTIVE OXIDATION OF ONE ALLOY COMPONENT

Selective oxidation will occur if only one oxide is stable. This is the case for alloys consisting of a noble metal such as Pt, Ag or Au, which does not form an oxide under normal conditions, and a reactive metal, which does. An example of this alloy class is Pt-Ni, which was analysed by Wagner [12]. It is also the case for more practically relevant alloy systems such as Fe-Cr and Ni-Cr, if the ambient oxygen potential is below the minimum necessary to form any iron or nickel bearing oxide but still above the value required for Cr₂O₃ formation.

In the case of exclusive scale formation, it is of interest to know whether the scaling rate is controlled by diffusion in the scale or in the alloy. In a formal sense, this question lacks meaning, as the rates at which B diffuses in the alloy and the scale must be in balance for a steady state to exist. However, it is reasonable to classify the process as being controlled by scale diffusion if the scale grows at the same rate as it does on pure B metal. Conversely, scaling is described as being controlled by alloy diffusion if the rate at which BO grows on the alloy is significantly less than on pure B metal. We therefore compare scaling rates on the two materials.

The growth rate of a NiO scale on a Pt-Ni alloy is proportional to the nickel cation flux in the oxide, given by Eq. [3.71], rewritten here as

$$J_{\text{Alloy}}^{\text{NiO}} = \text{constant} \left[\left(p''_{\text{O}_2} \right)^{\frac{1}{6}} - \left(p_{\text{O}_2}^{(i)} \right)^{\frac{1}{6}} \right] / X \quad [5.4]$$

where, as before, p''_{O_2} is the ambient oxygen partial pressure, and $p_{\text{O}_2}^{(i)}$ is the value at the alloy-scale interface. Doubly charged cation vacancies have been assumed, but a different charge can be accommodated by changing the exponent of p_{O_2} . Scale growth on pure nickel is related to the corresponding flux expression

$$J_{\text{Metal}}^{\text{NiO}} = \text{constant} \left[\left(p''_{\text{O}_2} \right)^{\frac{1}{6}} - \left(p_{\text{O}_2}^{(\text{eq})} \right)^{\frac{1}{6}} \right] / X \quad [5.5]$$

Here $p_{O_2}^{(eq)}$ represents the partial pressure for equilibrium between pure nickel and its oxide. The ratio of the two fluxes at a given scale thickness is therefore

$$\alpha = \frac{J_{\text{Alloy}}^{\text{NiO}}}{J_{\text{Metal}}^{\text{NiO}}} = \frac{\left(p''_{O_2}\right)^{\frac{1}{6}} - \left(p_{O_2}^{(i)}\right)^{\frac{1}{6}}}{\left(p''_{O_2}\right)^{\frac{1}{6}} - \left(p_{O_2}^{(eq)}\right)^{\frac{1}{6}}} \quad [5.6]$$

The boundary value oxygen pressures are next related to nickel concentrations.

The equilibrium condition for the reaction



is written

$$a_{\text{Ni}}^2 p_{O_2} = K_7^{-1} = p_{O_2}^{(eq)} \quad [5.8]$$

where pure nickel is the reference state, for which $a_{\text{Ni}} = 1$ and $p_{O_2}^{(eq)}$ has the standard equilibrium value. If the alloy is assumed to be ideal, we can write for the alloy-scale interface

$$N_{\text{Ni},i}^2 p_{O_2}^{(i)} = p_{O_2}^{(eq)} \quad [5.9]$$

where $N_{\text{Ni},i}$ denotes the nickel mole fraction at the alloy-scale interface. Since platinum is unreactive, it is possible to identify an alloy nickel level, $N_{\text{Ni},e}$, which will equilibrate with NiO and an oxygen partial pressure equal to the ambient value, p''_{O_2}

$$N_{\text{Ni},e}^2 p_{O_2}'' = p_{O_2}^{(eq)} \quad [5.10]$$

Substitution in Eq. [5.6] for $p_{O_2}^{(i)}$ and p_{O_2}'' from Eqs [5.9] and [5.10] leads to

$$\alpha = \frac{1 - (N_{\text{Ni},e}/N_{\text{Ni},i})^{\frac{1}{3}}}{1 - (N_{\text{Ni},e})^{\frac{1}{3}}} \quad [5.11]$$

Values of $N_{\text{Ni},e}$ are very low in the case of Pt-Ni alloys. Wagner [12] calculated values of 6×10^{-7} and 6×10^{-5} at 850 and 1100°C, for $p_{O_2}'' = 0.21$ atm. According to Eq. [5.11], then, $\alpha \approx 1$ and oxidation is controlled essentially by diffusion in NiO, if $N_{\text{Ni},i} \geq 0.01$. To make use of this finding, it is necessary to relate the interfacial mole fraction $N_{\text{Ni},i}$ to the original alloy level $N_{\text{Ni}}^{(o)}$.

The concentration at the interface is established by the diffusion of nickel towards the interface from the alloy and away from it into the oxide. Assuming that the alloy diffusion coefficient, \tilde{D} , is independent of composition, Fick's second law applies:

$$\frac{\partial N_{\text{Ni}}}{\partial t} = \tilde{D} \frac{\partial^2 N_{\text{Ni}}}{\partial x^2} \quad [5.12]$$

where x is the distance from the alloy surface and the initial condition

$$N_{\text{Ni}} = N_{\text{Ni}}^{(o)} \quad \text{for } t = o, x > o \quad [5.13]$$

applies. The problem is simplified considerably if movement of the alloy surface can be ignored. This will be a reasonable approximation if only a very thin oxide scale is formed, and alloy surface recession is consequently small. Diffusion within the alloy is then treated as the semi-infinite case (a limiting case of (Eq. [2.140]) in which $C_i = (C_o + C_1)/2$) with a fixed boundary, leading to the steady-state solution

$$N_{\text{Ni}} = N_{\text{Ni},i} + \left(N_{\text{Ni}}^{(o)} - N_{\text{Ni},i} \right) \operatorname{erf} \left(x / 2\sqrt{\tilde{D}t} \right) \quad [5.14]$$

The analysis is continued by enquiring as to what interfacial nickel concentration corresponds to an alloy flux sufficient to sustain NiO scale growth.

The flux of nickel toward the alloy surface is given by

$$J_{AB} = -\frac{\tilde{D}}{V_{AB}} \left[\frac{\partial N_{\text{Ni}}}{\partial x} \right]_{x=o} \quad [5.15]$$

where V_{AB} is the alloy molar volume. The differential is evaluated from Eq. [5.14], recalling the error function definition

$$\operatorname{erf}(z) = \frac{2}{\sqrt{\pi}} \int_0^z \exp(-\eta^2) d\eta \quad [5.16]$$

and obtaining

$$\frac{\partial N_{\text{Ni}}}{\partial x} = -\left(N_{\text{Ni}}^{(o)} - N_{\text{Ni},i} \right) \frac{1}{2\sqrt{\tilde{D}t}} \cdot \frac{2}{\sqrt{\pi}} \exp \left(-\frac{x}{2\sqrt{\tilde{D}t}} \right)^2 \quad [5.17]$$

Evaluation at $x = 0$, followed by substitution into Eq. [5.15] then yields

$$J_{AB} = \left(\frac{\tilde{D}}{\pi t} \right)^{\frac{1}{2}} \frac{\left(N_{\text{Ni}}^{(o)} - N_{\text{Ni},i} \right)}{V_{AB}} \quad [5.18]$$

To sustain external scale growth, this flux must equal the rate at which nickel is incorporated into the growing scale,

$$J_{AB} = \frac{d(n_{\text{Ni}}/A)}{dt} \quad [5.19]$$

where n_{Ni}/A represents the number of moles of nickel in the scale per unit surface area. This rate is found from scale thickening

$$d(n_{\text{Ni}}/A) = d(X/V_{\text{NiO}}) \quad [5.20]$$

and since $X^2 = 2k_p t$,

$$\frac{d(n_{\text{Ni}}/A)}{dt} = \frac{1}{V_{\text{NiO}}} \left(\frac{k_p}{2t} \right)^{1/2} \quad [5.21]$$

Combining Eq. [5.18], [5.19] and [5.21], we obtain

$$\left(N_{\text{Ni}}^{(o)} - N_{\text{Ni},i} \right) = \frac{V_{AB}}{V_{\text{NiO}}} \left(\frac{\pi k_p}{2\tilde{D}} \right)^{1/2} \quad [5.22]$$

Wagner pointed out that the maximum flux available from the alloy was delivered if $N_{\text{Ni},i} \approx 0$, and this enables the calculation from Eq. [5.22] of a minimum level of $N_{\text{Ni}}^{(o)}$ necessary to sustain external scale growth. This point is discussed further below.

The approximation used above of a zero rate of scale-alloy interface movement can be avoided, and the moving boundary incorporated into the description. The interface movement is related to the scaling rate by (Eq. [1.29]), using V_{AB} in place of V_M . The position of the alloy-scale interface relative to its original location, Δx_M , is given by

$$\Delta x_M = (2\alpha k_c^\circ t)^{1/2} \quad [5.23]$$

where k_c° is the corrosion rate constant for pure nickel and $\alpha = k_c/k_c^\circ$. The mass balance of Eqs [5.21] and [5.22] is then replaced by a balance for platinum, which is rejected from the oxide and diffuses from the scale-alloy interface into the alloy.

The amount of platinum (per unit surface area) made available when the interface advances by an increment dy is equal to $(1 - N_{\text{Ni},i})dy$. The rate at which that occurs is equated to the diffusion rate, which is given by Fick's first law, evaluated at the interface. Thus

$$(1 - N_{\text{Ni},i}) \frac{dy}{dt} = -\tilde{D} \frac{\partial(1 - N_{\text{Ni}})}{\partial x} \Big|_{x=y} \quad [5.24]$$

assuming that the alloy molar volume is independent of composition.

Wagner found the result

$$\frac{N_{\text{Ni}}^{(o)} - N_{\text{Ni},i}}{1 - N_{\text{Ni},i}} = F(k_c/2\tilde{D})^{1/2} \quad [5.25]$$

where the function $F(u)$ is defined by

$$F(u) = \pi^{1/2} u (1 - \operatorname{erf} u) \exp(u^2) \quad [5.26]$$

Thus $N_{\text{Ni},i}$ and α can be found from the simultaneous solution of Eq. [5.11] and [5.25]. It is useful to observe that when $u \gg 1$, $F(u) \approx 1$ and when $u \ll 1$, $F(u) \approx \pi^{1/2}u$.

If k_c is small enough, then $u \ll 1$. In this case of negligible interface recession, the solution Eq. [5.25] reduces to the form Eq. [5.22], obtained on the basis that the interface movement can be ignored. In any event, the analysis predicts that scale growth is controlled by oxide diffusion ($k_c = k_c^\circ$) if $N_{\text{Ni}} > N_{\text{Ni,min}}$, and by alloy

diffusion if $N_{\text{Ni}} < N_{\text{Ni,min}}$. In the former case, $\alpha = k_c/k_c^o$ is independent of $N_{\text{Ni}}^{(o)}$, and in the latter case, α decreases as $N_{\text{Ni}}^{(o)}$ is lowered.

Comparison of experimental results [13] for the dependence of α on $N_{\text{Ni}}^{(o)}$ with Wagner's predictions for the Pt-Ni system showed that the latter were reasonably successful in the regime where $N_{\text{Ni}}^{(o)} < 0.5$ and alloy diffusion controlled the scaling rate ($\alpha < 1$). However, at higher nickel levels, the measured rates were significantly slower than predicted. As a result, the predicted critical values of N_{Ni}^o at which rate control should transfer to scale diffusion (0.7 at 850°C and 0.6 at 1100°C) were incorrect. However, the significant errors in measured values of k_c and \tilde{D} lead to large compounded errors in k_c/\tilde{D} , and the accurate calculation of Eq. [5.25] is therefore difficult. Moreover, the assumption that NiO scale growth is controlled by lattice diffusion is not applicable at temperatures lower than about 900°C, where grain boundary diffusion is more important.

In the case where $u = (k_c/2\tilde{D})^{\frac{1}{2}} \ll 1$, ie, when scale-alloy interface movement is slow compared to alloy diffusion, then

$$F(u) \approx \pi^{\frac{1}{2}} u \quad [5.27]$$

Substitution into Eq. [5.25] then yields

$$N_{\text{Ni},i} = \frac{N_{\text{Ni}}^{(o)} - \left(\frac{\pi k_c}{2\tilde{D}}\right)^{\frac{1}{2}}}{1 - \left(\frac{\pi k_c}{2\tilde{D}}\right)^{\frac{1}{2}}} \quad [5.28]$$

This approximation is not applicable to the Pt-Ni alloy situation, because the NiO growth rate leads to relatively high k_c values. It might be appropriate, however, for slower growing oxides such as Cr₂O₃ and Al₂O₃. Data on several alloys collected by Whittle et al. [14] are reproduced in Table 5.2, along with data for Ni-Al [15,16]. It is seen that the condition $u \ll 1$ is met in these cases. Interface concentrations calculated from Eq. [5.28] are also shown in the table.

The extent of depletion predicted from Eq. [5.28] is, in fact, unrealistically small. Chromium concentration profiles measured in an Fe-32Cr alloy after selective formation of a Cr₂O₃ scale are shown in Fig. 5.9. These confirm that depletion occurs but show that the effect is much greater than predicted. Given the sensitivity of the calculation to errors in k_c and \tilde{D} , this is perhaps not surprising. We note in particular that \tilde{D} will normally be a function of alloy composition (Section 2.7). Bastow et al. [18] showed that an interfacial value $N_{\text{Cr},i} = 0.19$, in approximate agreement with their EPMA measurement, was consistent with a rate constant $k_c = 3.9 \times 10^{-12} \text{ cm}^2 \text{ s}^{-1}$, a value three times faster than the rate they actually observed. This discrepancy has led to a more

TABLE 5.2 Kinetic Parameters for Alloy Diffusion and Selective Scale Growth [14]

Alloy	$N_A^{(o)}$	T/°C	$\tilde{D}_{AB}/\text{cm}^2 \text{s}^{-1}$	$k_c/\text{cm}^2 \text{s}^{-1}$	u	$N_{A,i}$ (Eq [5.28])
Ni-28Cr	0.30	1000	4.1×10^{-11}	1.2×10^{-13}	3.8×10^{-2}	0.24
		1200	3.9×10^{-10}	7.2×10^{-13}	3.0×10^{-2}	0.26
Fe-28Cr	0.29	1000	4.1×10^{-10}	1.2×10^{-12}	3.8×10^{-2}	0.24
		1200	3.9×10^{-9}	3.9×10^{-12}	2.2×10^{-2}	0.26
Fe-4.4 Al	0.087	1000	8.4×10^{-9}	2.6×10^{-16}	1.8×10^{-4}	0.087
		1200	2.1×10^{-6}	1.4×10^{-13}	1.8×10^{-4}	0.087
Fe-12 Al	0.22	1000	8.4×10^{-9}	2.0×10^{-18}	1.2×10^{-5}	0.22
		1200	2.1×10^{-6}	6.4×10^{-16}	1.2×10^{-5}	0.22
Ni-10 Al	0.19	1200	1×10^{-9} [16]	4.0×10^{-13} [15]	1.4×10^{-2}	0.17

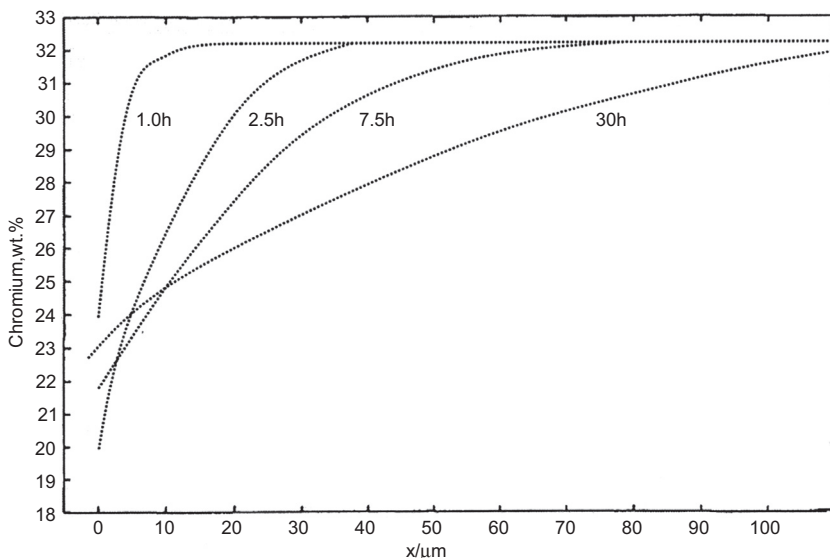


FIGURE 5.9 Chromium depletion in Fe-32Cr measured by electron probe microanalysis after selective oxidation of chromium at $T = 977^\circ\text{C}$. Reprinted from G.L. Wulf, M.B. McGinn, G.R. Wallwork, *Corros. Sci.* 9 (1969) 739, with permission from Elsevier.

detailed examination of the relationship between alloy and scale diffusion, which we discuss below. First, however, an examination of qualitative trends revealed by the data in Table 5.2 is useful.

Comparing iron and nickel-base chromia-forming alloys, it is seen that the ratio k_c/\tilde{D} is somewhat greater for the latter. This reflects mainly the fact that diffusion in austenite is slower than in ferrite. Consequently, the chromium concentration at the alloy-oxide interface will be depleted to a lower value in a Ni-Cr alloy than in an equivalent Fe-Cr alloy under the same conditions. Comparing Fe-Cr and Fe-Al alloys, it is seen that the ratio k_c/\tilde{D} is much smaller in the alumina forming alloys, because the oxidation rate is much slower and alloy diffusion is faster. As a result, Fe-Al alloys are predicted to maintain rather flat aluminium concentration profiles, with $N_{\text{Al},i} \approx N_{\text{Al}}^{(o)}$. This has been verified [19] for Fe-Cr-Al alloys under circumstances where a scale of alumina only forms. Microprobe analysis, with a spatial resolution of 1–2 μm , showed no detectable variation in the alloy aluminium level from the alloy interior to the alloy-scale interface. Thus any depletion zone was of a thickness less than 1–2 μm . The Ni-Al alloys have k_c/\tilde{D} values lower than either Ni-Cr or Fe-Cr, leading to a reduced extent of depletion. In comparison to Fe-Al alloys, however, Ni-Al is subject to significantly more depletion.

TABLE 5.3 Values of $N_{B,\min}$ to Support Selective Oxide Scale Growth

Alloy	Scale	T/°C	Predicted (Eq [5.25])	Observed	Refs
Ni-Cr	Cr ₂ O ₃	1000	0.07	0.15	[7]
Fe-Cr	Cr ₂ O ₃	1000	0.07	0.14	[7]
Ni-Al	Al ₂ O ₃	1200	0.02	0.12–0.24	[15,20,21]
Fe-Al ^a	Al ₂ O ₃	1300	10 ⁻⁴	0.02–0.04	[22]

^aObserved on Fe-Cr-Al alloys growing scales of Al₂O₃ only.

Values of the minimum concentration, $N_{B,\min}$, of the scale-forming element necessary to support external scale growth were calculated from Eq. [5.22] and are listed in Table 5.3. Comparison with experimental observations of $N_{B,\min}$, however, reveals that these predictions are not useful. As already noted, one reason for this lack of success is the sensitivity of the calculation to error in the basic data used, k_c and \tilde{D} . An example is shown in Fig. 5.10, where calculations [18] for Fe-Cr, assuming two values for \tilde{D} (which differ by a factor of two), are seen to result in values of $N_{Cr,i}$ which differ by 0.05, ie, 40%. A further reason for its lack of quantitative success in predicting values of $N_{B,\min}$,

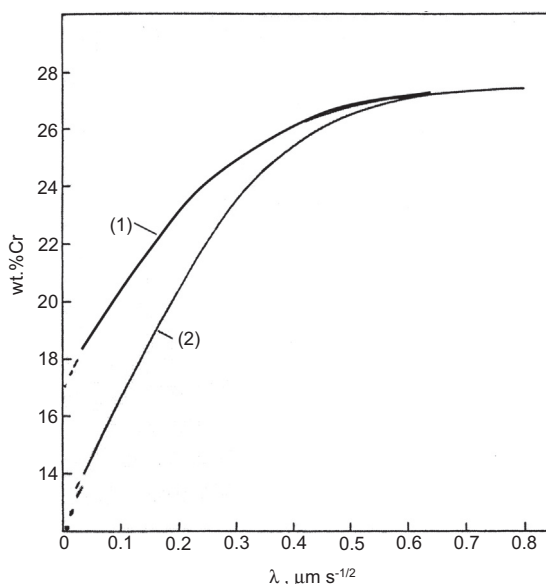


FIGURE 5.10 Chromium depletion profiles calculated for $D_{FeCr} = 1 \times 10^{-12}$ and $2 \times 10^{-12} \text{ cm}^2 \text{ s}^{-1}$, in the case of Fe-27.4 Cr oxidised at 1000°C [18]. With kind permission from Springer Science and Business Media.

is that Wagner's treatment was designed to assess the minimum alloy concentration necessary to supply a flux to the surface sufficient to sustain the growth of a single-phase scale presumed to have formed already. Thus the theory does not provide guidance on how much of the alloy component is required to form this scale in the first place. Before returning to this question, we consider again the depletion profiles in Fig. 5.9.

5.5 SELECTIVE OXIDATION OF ONE ALLOY COMPONENT UNDER NONSTEADY-STATE CONDITIONS

Although concentration measurements near a phase boundary are subject to error, it seems from Fig. 5.9 that $N_{Cr,i}$ first decreases then increases with time. Although $N_{Cr,i}$ ultimately reaches a constant value, the steady-state assumption of fixed boundary conditions is apparently inapplicable for a significant period at the commencement of reaction. The steady-state assumption is the basis for Wagner's analytical solution Eq. [5.25], which could for this reason be inapplicable.

The nonsteady-state situation has been analysed for Fe-Cr oxidation by Whittle et al. [14], Wulf et al. [17] and Bastow et al. [18], using a finite difference method. In this numerical approach, it is possible to allow for a composition-dependent alloy diffusion coefficient, but this has been shown to have little effect on the interfacial concentration in Fe-Cr alloys.

The possible variation in $N_{Cr,i}$ with time is reflected in the mass balance for chromium at the alloy-scale interface. The situation is shown schematically for a binary alloy AB in Fig. 5.11, where C represents concentration (moles/volume), and an average value, $C_{B,OX}$, is specified for B in the scale of BO_x . The general statement of mass balance at a moving interface is written

$$J_{AB} - J_B^{OX} = v \left(C'_{B,OX} - C_{B,i} \right) \quad [5.29]$$

where J_B^{OX} is the flux of B away from the interface into the oxide, v is the velocity of the interface and $C'_{B,OX}$ is the boundary value of C_B in the oxide at the interface. All of J_{AB} , J_B^{OX} and v must be defined in the same frame of reference (Section 2.7). The choice is arbitrary, but the solution of the diffusion profile in the alloy is facilitated by using a reference frame with its origin at the original alloy surface, marked by a dashed line in Fig. 5.11. The displacement of the scale-alloy interface from its origin is specified as x_c , and hence $v = dx_c/dt$. The flux of B from the alloy toward the interface is given by

$$J_{AB} = -D_{AB} \frac{\partial C_B}{\partial x} \Big|_{x=x_c} \quad [5.30]$$

Component B also diffuses away from the interface through the scale, allowing it to grow. This is normally expressed with respect to a reference

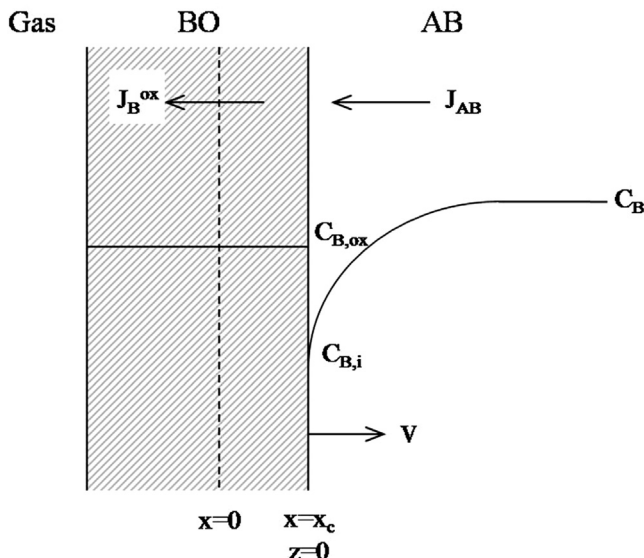


FIGURE 5.11 Mass transfer at moving scale-alloy interface.

frame with its origin at the metal-scale interface. Defining the scale thickness as z_s , then

$$V_{BO_v} (J_B^{OX})' = \frac{dz_s}{dt} \quad [5.31]$$

or

$$(J_B^{OX})' = C_{B,OX} \frac{dz_s}{dt} \quad [5.32]$$

where the prime is used to denote the different frame of reference, z . This is transformed to the desired reference frame, x , using the relationship

$$J_B^{OX} = (J_B^{OX})' + C_{B,OX} v_{1,2} \quad [5.33]$$

where $v_{1,2}$ is the velocity of the oxide frame with respect to the original alloy surface

$$v_{1,2} = dx_c/dt \quad [5.34]$$

Combination of the Eqs [5.29]–[5.34] leads to

$$-D \left. \frac{\partial c_B}{\partial x} \right|_{x=x_c} - C_{B,OX} \left(\frac{dz_s}{dt} - \frac{dx_c}{dt} \right) = \frac{dx_c}{dt} (C_{B,OX} - C_{B,i}) \quad [5.35]$$

where the approximation $C'_{B,OX} \approx C_{B,OX}$ has been used. Noting that

$$z_s = \frac{V_{BO_v}}{V_{AB}} x_c \quad [5.36]$$

it is found from Eq. [5.35] that

$$-D_{AB} \frac{\partial c_A}{\partial x} \Big|_{x=x_c} = \frac{dx_c}{dt} \left(\frac{V_{MO_v}}{V_{AB}} C_{B,OX} - C_{B,i} \right) \quad [5.37]$$

Numerical solution of Eq. [5.15] and [5.37], together with an expression for the alloy recession rate

$$\frac{dx_c}{dt} = \frac{V_{AB}}{V_{BO_v}} \frac{dz_s}{dt} \quad [5.38]$$

coupled with a rate law $z_s = f(t)$, then reveals the alloy depletion profiles.

Whittle et al. [14] proposed that an appropriate formulation of the rate law was

$$z^2 = 2k_p t + k \quad [5.39]$$

which differs from that of Wagner. Their evaluation of the change with time of the interfacial concentration relative to the bulk alloy value,

$$\theta = N_{B,i}/N_B^{(o)} \quad [5.40]$$

is shown in Fig. 5.12 for a model alloy. It is seen that a rapid decrease in $N_{B,i}$ occurs in the initial stages of reaction, when the oxide growth flux, (and rate at which B is withdrawn) is maximal. This initial decrease is followed by an

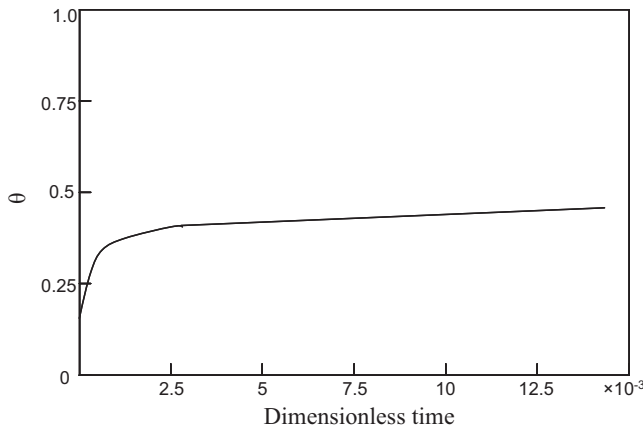


FIGURE 5.12 Calculated variation of interfacial concentration with time during nonsteady-state oxidation. Reprinted from D.P. Whittle, D.J. Evans, D.B. Scully, G.C. Wood, *Acta Met.* 15 (1967) 1421, with permission from Elsevier.

increase, until a steady-state value is reached. This theoretical prediction is in agreement with experimental observation for the Fe-Cr system. Thus we conclude that the steady state assumed by Wagner is in fact arrived at, but that during an initial period, this is not the case.

The existence of a steady-state is actually a prerequisite for parabolic kinetics to be in effect. As seen in Section 3.7, diffusion-controlled scale growth leads to parabolic kinetics only if the boundary conditions are fixed with time. The boundary values in a scale are related to the alloy interfacial composition through a local equilibrium condition such as Eq. [5.10]. More generally

$$\frac{2}{v} \underline{B} + O_2 = \frac{2}{v} BO_v, \quad \Delta G_{41}^\circ \quad [5.41]$$

$$\left(a_B^{2/v} p_{O_2} \right)^{-1} = K_{41} = \exp(-\Delta G_{41}^\circ / RT) \quad [5.42]$$

If the activity coefficient for B is denoted by γ , then

$$p_{O_2}^{(i)} = (K_{41})^{-1} / (\gamma N_{B,i})^{2/v} \quad [5.43]$$

and, in general, rate expressions such as Eq. [5.4] lead to parabolic kinetics only if $N_{B,i} \neq f(t)$. Conversely, the observation of parabolic kinetics is an indication that $N_{B,i}$ is constant. However, if $p_{O_2}^{(i)} \ll p_{O_2}''$, the effect on oxidation rate of transient variation in $N_{B,i}$ could be small, as seen from Eq. [5.4].

The initial time dependence of $N_{B,i}$ predicted by Whittle et al. [14] was a consequence of their use of Eq. [5.39] to describe scaling kinetics. As seen from the differential form

$$\frac{dz_s}{dt} = \frac{k_p}{(2k_p t + k)^{\frac{1}{2}}} \quad [5.44]$$

the deviation from parabolic kinetics is greatest in the early stages of reaction, when $2k_p t < k$. A non-zero value for k is realistic, reflecting the existence of an oxide film on the metal surface prior to commencement of the high-temperature reaction. Even in the absence of such a preformed oxide, strictly parabolic kinetics cannot obtain at extremely short times. If $k = 0$, then dz_s/dt is predicted to approach infinity as t approaches zero, an impossibility, as diffusion from the alloy is limited. It is recognised that the very initial kinetics cannot be parabolic, just as the exclusive oxidation of only one alloy component when the ambient p_{O_2} is sufficient to oxidise others is initially impossible. This initial period of reaction, referred to as ‘transient’ because it precedes the establishment of steady-state conditions, is discussed further in Section 5.7.

Other oxidation morphologies result if selective oxidation of one component to form an external scale does not occur. Their natures vary with the reactivity of other alloy components. If no other alloy metals are reactive at the oxidant activity and temperature in question, and the one reactive component

cannot reach the surface quickly enough to develop a scale, then internal oxidation results. This situation is considered in Chapter 6. Another reactive alloy component will oxidise simultaneously. Oxides which have limited intersolubility develop as separate phases, a situation described in Chapter 7. However, if the degree of intersolubility is large, it is still possible that a single-phase external scale of solid solution oxide can result. The questions of interest then concern the nature of this scale, its growth rate and how these properties vary with alloy composition.

5.6 SOLID SOLUTION OXIDE SCALES

Pairs of binary oxides, $AO_{v_1} + BO_{v_2}$, will dissolve in one another to an extent which is greater if (1) $v_1 = v_2$, (2) the oxides are crystallographically isotypic, (3) the cations A^{2v_1+} and B^{2v_2+} are similar in size and polarisability and (4) the stabilities of the oxides are not too different. The oxides MnO, FeO, CoO and NiO, all of which have the face-centred cubic NaCl structure, form ternary solid solutions $A_{1-\xi}B_\xi O$ in which $O \leq \xi \leq 1$. Similarly, $\alpha\text{-Fe}_2\text{O}_3$ and Cr_2O_3 , both of which have a hexagonal crystal structure, are completely miscible at high temperatures. In the same way, FeS and NiS are fully intersoluble, as are FeS and CoS: all three monosulphides have the hexagonal NiAs structure. In general, the ratio $N_A/N_B = (1 - \xi)/\xi$ in the oxide differs from the corresponding alloy ratio because the more reactive metal enters the scale preferentially. Furthermore, as the cation self-diffusion coefficients in the oxide, D_A and D_B , will differ, the cation ratio will vary with position in the scale. To calculate the scale growth rate as a function of alloy composition, it is necessary to know the distributions of the two metals within the scale. This problem has been analysed by Wagner [23] and the results extended by Coates and Dalvi [24].

The coordinate systems shown in Fig. 5.11 are again employed. The z frame, attached to the alloy-scale interface, is used to describe transport in the oxide: the x frame, with its origin at the original alloy surface, describes transport in the alloy. Of course it is understood that the oxide concentration profile will, in general, not be flat. The molar flux of each cation species in the oxide, J_i , is given by

$$J_i = -D_i C_i \frac{\partial \ln a_i}{\partial z} \quad [5.45]$$

where i is A or B , and kinetic cross-effects are ignored. The Gibbs Equation (Eq. [2.9]) relates the chemical potentials of the binary oxides and their constituents

$$\mu_A^o + RT \ln a_A + \frac{z_A}{z_O} (\mu_O^o + RT \ln a_O) = \mu_{AO_v}^o + RT \ln a_{AO_v} \quad [5.46]$$

with a similar equation for BO_v . Assuming for the sake of simplicity that the valences, z_i , are related by

$$z_A = z_B = |z_O| = 2 \quad [5.47]$$

so that $v = 1$, one obtains from Eqs [5.45] and [5.46]

$$J_A = \frac{D_A(1-\xi)}{V_{OX}} \left(\frac{\partial \ln a_{AO}}{\partial \xi} \frac{\partial \xi}{\partial z} - \frac{\partial \ln a_O}{\partial z} \right) \quad [5.48]$$

$$J_B = -\frac{D_B \xi}{V_{OX}} \left(\frac{\partial \ln a_{BO}}{\partial \xi} \frac{\partial \xi}{\partial z} - \frac{\partial \ln a_O}{\partial z} \right) \quad [5.49]$$

It is supposed that V_{OX} does not vary with ξ and that $\partial \ln a_{AO}/\partial \xi$ and $\partial \ln a_{BO}/\partial \xi$ are known from the solution thermodynamics of the mixed oxide. The scale-thickening rate is then found from

$$(J_A + J_B)V_{OX} = \frac{dz_s}{dt} = \frac{k_p}{z_s} \quad [5.50]$$

where z_s is the instantaneous scale thickness. Because diffusion control is in effect, the system is in a steady state, and both ξ and a_o can be expressed in terms of a normalised position parameter

$$y = z/z_s \quad [5.51]$$

Substitution from Eqs [5.48], [5.49] and [5.51] into Eq. [5.50] yields

$$D_A(1-\xi) \left(-\frac{\partial \ln a_{AO}}{\partial \xi} \frac{\partial \xi}{\partial y} + \frac{\partial \ln a_o}{\partial y} \right) + D_B \xi \left(-\frac{\partial \ln a_{BO}}{\partial \xi} \frac{\partial \xi}{\partial y} + \frac{\partial \ln a_o}{\partial y} \right) = k \quad [5.52]$$

Application of the continuity condition for the diffusion of one component on the basis again that ξ and a_o are functions of y only leads to

$$yk \frac{\partial \xi}{\partial y} = -\frac{d}{dy} \left[D_B \xi \left(\frac{\partial \ln a_{BO}}{\partial \xi} \frac{\partial \xi}{\partial y} - \frac{\partial \ln a_o}{\partial y} \right) \right] \quad [5.53]$$

Each of Eqs [5.52] and [5.53] apply only within the scale.

Within the alloy phase, the distribution of component B is found by solving Fick's second law

$$\frac{\partial N_B}{\partial t} = D_{AB} \frac{\partial^2 N_B}{\partial x^2} \quad [5.54]$$

assuming D_{AB} to be a constant. Using the Boltzmann transformation

$$\lambda = x/t^{1/2} \quad [5.55]$$

we obtain the ordinary differential equation

$$D_{AB} \frac{d^2 N_B}{d \lambda^2} + \frac{\lambda}{2} \frac{d N_B}{d \lambda} = 0 \quad [5.56]$$

Solution of the three simultaneous Eqs [5.52]–[5.54] requires appropriate boundary conditions. These are provided by the initial conditions

$$N_B = N_B^{(o)} \text{ for } x > o, t = o; x = \infty, t > o \quad [5.57]$$

and

$$a_o(y = 1) = a_o'' \quad [5.58]$$

together with the thermodynamic relationships

$$\xi(y = 1) = f_1(a_o'') \quad [5.59]$$

$$\xi(y = o) = f_2(N_{B,i}) \quad [5.60]$$

$$a'_o = f_3(\xi') \quad [5.61]$$

and the mass balances which apply at the scale interfaces. The mass balance for B at the scale-gas interface is

$$J_B(y = 1) = \frac{\xi''}{V_{OX}} \frac{dz_s}{dt} \quad [5.62]$$

which, upon substitution from Eqs [5.51]–[5.53], becomes

$$-D_B \xi \left(\frac{\partial \ln a_{BO}}{\partial \xi} \frac{d\xi}{dy} - \frac{d \ln a_o}{dy} \right) \Big|_{y=1} = \xi'' k \quad [5.63]$$

Similarly, a mass balance for B at the scale-alloy interface ($y = 0$) is used to evaluate ξ' . Wagner treated this by relating the average mole fraction of B in the scale, ξ_{AV} , to the amount consumed from the alloy.

Using the valences of Eq. [5.47], his result can be written:

$$N_{B,i} + \frac{2\frac{3}{2}D_{AB}V_{OX}}{k^{\frac{1}{2}}V_{AB}} \left(\frac{dN_B}{d\lambda} \right)_{\lambda=x_s/t^{\frac{1}{2}}} = - \left[\frac{D_B \xi}{k} \left(\frac{\partial \ln a_{BO}}{\partial \xi} \frac{d\xi}{dy} - \frac{d \ln a_o}{dy} \right) \right]_{y=0} \quad [5.64]$$

Coates and Dalvi extended the range of applicability of this treatment by including dissolution of oxygen in the alloy and its diffusion into that phase. Even without that complication, it will be appreciated that solution of the simultaneous Eqs [5.52]–[5.54] together with the mass balances Eqs [5.63] and [5.64] represents a substantial undertaking. Since, moreover, the diffusional properties of the oxide can be expected to vary with both ξ and a_o , a solution is essentially impossible without a relatively simple diffusion model.

5.6.1 Modelling Diffusion in Solid Solution Scales

A fruitful approach was proposed by Dalvi and Coates [25] using the data [26] shown in Fig. 5.13 for the distribution of nickel and cobalt in a

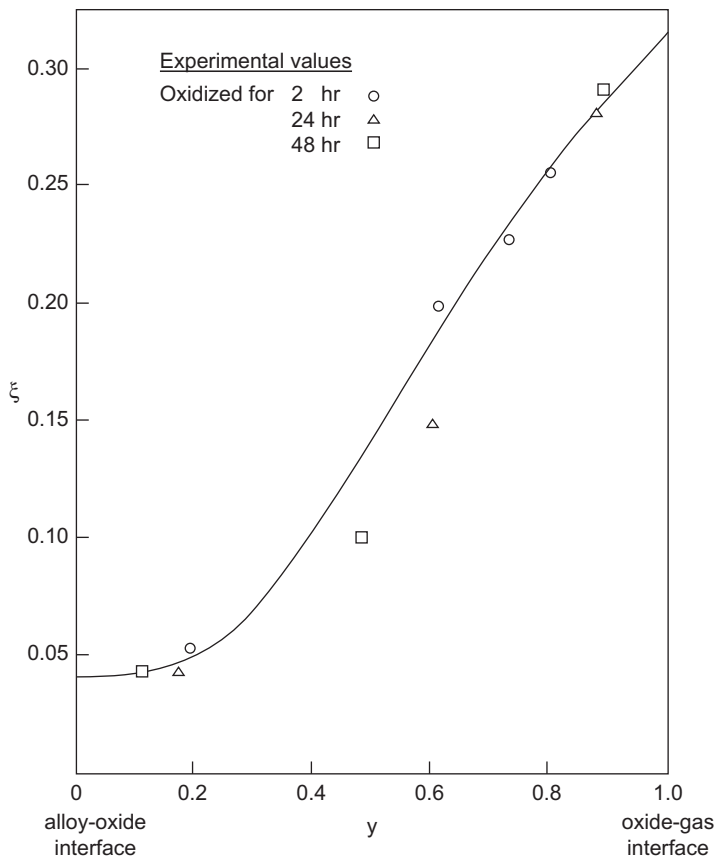


FIGURE 5.13 Distribution of CoO in CoO-NiO solid solution scale grown on Ni-10.9Co at 1000°C. Experimental data [26] are compared with model curve calculated [25] from Eqs [5.77] and [5.78] [25]. With kind permission from Springer Science and Business Media.

(Ni, Co) O scale grown on a binary alloy. The mixed oxide is a nearly ideal solution

$$\frac{d \ln a_{\text{CoO}}}{d \ln \xi} = 1 \quad [5.65]$$

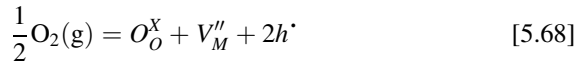
and the Gibbs-Duhem equation can be written

$$d \ln a_{\text{NiO}} = - \frac{\xi}{1 - \xi} d \ln a_{\text{CoO}} \quad [5.66]$$

Substitution from these thermodynamic equations into Eq. [5.52] leads to

$$(D_{\text{Ni}} - D_{\text{Co}}) \frac{d\xi}{dy} + \frac{d \ln a_o}{dy} [(1 - \xi)D_{\text{Ni}} + \xi D_{\text{Co}}] = k \quad [5.67]$$

Investigations into the NiO-CoO solid solution by Zintl [27,28] revealed that the vacancy mole fraction, N_V , decreased almost exponentially with additions of NiO. Based on this finding and the vacancy model for each of CoO and NiO



Wagner [29] suggested that N_V in the solid solution oxide could be modelled as

$$N_V = N_V^{\text{NiO}} \beta^\xi p_{\text{O}_2}^{\frac{1}{6}} \quad [5.69]$$

reflecting a law of mixtures for the free energy of vacancy formation via Eq. [5.68], ie,

$$\Delta G_V^\circ = (1 - \xi) (\Delta G_V^\circ)_{\text{NiO}} + \xi (\Delta G_V^\circ)_{\text{CoO}} \quad [5.70]$$

Here

$$\beta = N_V^{\text{CoO}} / N_V^{\text{NiO}} \quad [5.71]$$

and N_V^{MO} is the vacancy mole fraction in the indicated binary oxide at $p_{\text{O}_2} = 1 \text{ atm}$.

Recalling that for substitutional diffusion with $N_M \approx 1$, $D_M = D_V N_V$, it was further suggested [29] that diffusion in the ternary oxide could be described by

$$D_{\text{Co}} = D_{\text{Co}}^o (N_V / N_V^{\text{CoO}}) \quad [5.72]$$

and

$$D_{\text{Ni}} = D_{\text{Ni}}^o (N_V / N_V^{\text{NiO}}) \quad [5.73]$$

where D_M^o denotes the diffusion coefficient of the indicated metal in its pure binary oxide at $p_{\text{O}_2} = 1 \text{ atm}$. Combination of Eqs [5.69], [5.72] and [5.73] with the definition

$$p = D_{\text{Ni}} / D_{\text{Co}} \quad [5.74]$$

then leads to

$$D_{\text{Co}} = D_{\text{Co}}^o \beta^{\xi-1} p_{\text{O}_2}^{\frac{1}{6}} \quad [5.75]$$

$$D_{\text{Ni}} = p D_{\text{Co}}^o \beta^{\xi-1} p_{\text{O}_2}^{\frac{1}{6}} \quad [5.76]$$

Substitution from Eqs [5.75] and [5.76] into Eq. [5.67] yields

$$\frac{d \ln a_o}{dy} = \left\{ \frac{k'}{\beta^{\xi-1} p_{\text{O}_2}^{\frac{1}{6}}} - (p-1) \frac{d\xi}{dy} \right\} / [p - (p-1)\xi] \quad [5.77]$$

where $k' = k / D_{\text{Co}}^o$. Application of this diffusion model to the scale-gas interface mass balance Eq. [5.63] yields, after some algebra, a differential

equation describing the variation within the scale of ξ with normalised position y

$$\theta \frac{d^2\xi}{dy^2} + \left\{ \left(1 - \frac{1}{6} \right) (p - 1) + \theta \ln \beta \right\} \left(\frac{d\xi}{dy} \right)^2 + \beta^{\xi''-\xi} \left(\frac{a_o''}{a_o} \right)^{\frac{1}{6}} \left\{ \frac{p(1 - \frac{1}{6}) - y\theta^2}{\xi''(1 - \xi'')(p - 1)} \right\} \left(\frac{d\xi}{dy} \right)_{y=1} \left(\frac{d\xi}{dy} \right) = 0 \quad [5.78]$$

where $\theta = p - (p - 1)\xi$.

Simultaneous solution of Eqs [5.77] and [5.78] using measured values of p and β then yields ξ and a_o as functions of y . It was found expedient to treat the exponent of oxygen activity appearing in the defect equilibrium Eq. [5.69] as a variable. When $p_{O_2}^{\frac{1}{3}}$ was used, the calculated composition profiles shown in Fig. 5.13 were found to fit the experimental data very well. The index $\frac{1}{3}$ was interpreted as corresponding to a mixture of singly and doubly charged vacancies. The cobalt enrichment at the scale surface resulted from the fact that $p = D_{Ni}/D_{Co} \approx 0.5$.

Single-phase (FeMn)O scales grow according to parabolic kinetics on Fe-Mn alloys oxidised in CO₂-CO atmospheres [30]. Microprobe concentration profiles showed that the scale compositions were rather uniform, and approximately the same as the alloy compositions. This reflects the fact that diffusion in the oxide was about 10⁴ times faster than in the alloy. The relatively flat, linear gradients in the scale could be approximated by

$$\frac{d\xi}{dy} = b \quad [5.79]$$

and the ideality of the FeO-MnO solution [31] allowed use of Eq. [5.65]. In this case, Eqs [5.53] and [5.63] yield the simple result

$$D_{Mn} = pD_{Fe} = \frac{k\xi''(p - 1)(1 - \xi'')}{b} \quad [5.80]$$

after elimination of $\partial \ln a_o / \partial y$. This yielded a value of $p = 0.99$, consistent with the lack of segregation of the metals within the scale. The diffusion coefficient of iron in wüstite is proportional to the oxide nonstoichiometry [32], and an equation analogous to Eq. [5.72] applies to the (Fe, Mn)O scale. Values of D_{Fe} deduced from the alloy scaling rates were used (in Eq. [5.72]) to calculate the nonstoichiometry of the mixed oxide. Fig. 5.14 compares the calculated results with those measured for powdered oxide after equilibrating with the gas. The good agreement provides additional support for the validity of the diffusion model.

Similar analyses have been carried out for solid-solution oxide scales developed on Co-Fe [33,34] and Ni-Fe [35] alloys and for monosulphide scales on Fe-Ni [36,37] and Fe-Co [38,39]. An unusual pattern of component

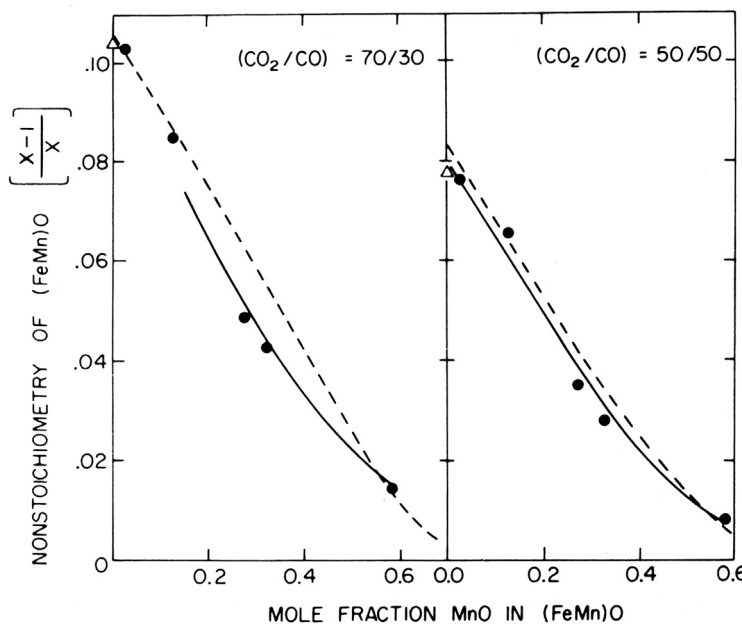


FIGURE 5.14 Nonstoichiometry of $(\text{Fe}, \text{Mn})_{1-\delta}\text{O}$: points deduced from alloy scaling rates and Eq. [5.72]; dashed curves measured by equilibrating powdered oxides with gas [30]. Reproduced by permission of The Electrochemical Society.

segregation was found in the $(\text{Co}, \text{Fe})\text{O}$ scales, where at low ambient p_{O_2} values, the more mobile iron was enriched towards the scale surface, as seen in Fig. 5.15A. However, at high p_{O_2} values, a maximum in iron concentration developed in the scale interior (Fig. 5.15B). The explanation for this is the curious variation in $p = D_{\text{Fe}}/D_{\text{Co}}$ with a_o , as measured by Crow [40] and shown in Fig. 5.15C. Incorporating this information into the numerical solution procedure for Eqs [5.77] and [5.78] allowed Narita et al. [41] to calculate the scale concentration profile successfully (Fig. 5.15A and B). The reason for the change in p with a_o is not apparent. It has been suggested by Whittle et al. [42] that correlation effects can lead to variation of p with vacancy concentration, and hence with a_o . However, even this model cannot account for the reversal in relative mobilities of iron and cobalt evident in Fig. 5.15.

Sulphide scales provide the investigator with the advantage of being able to measure accurate concentration profiles for the oxidant species using an electron microprobe. Results for an $(\text{Fe}, \text{Ni})_{1-\delta}\text{S}$ scale are shown in Fig. 5.16, where the sulphur concentration varies with position in a nonmonotonic fashion. The mixed sulphide grew at a faster rate than $\text{Fe}_{1-\delta}\text{S}$ scales grew at the same p_{S_2} on pure iron. The indicated enhancement in D_{Fe} could arise either

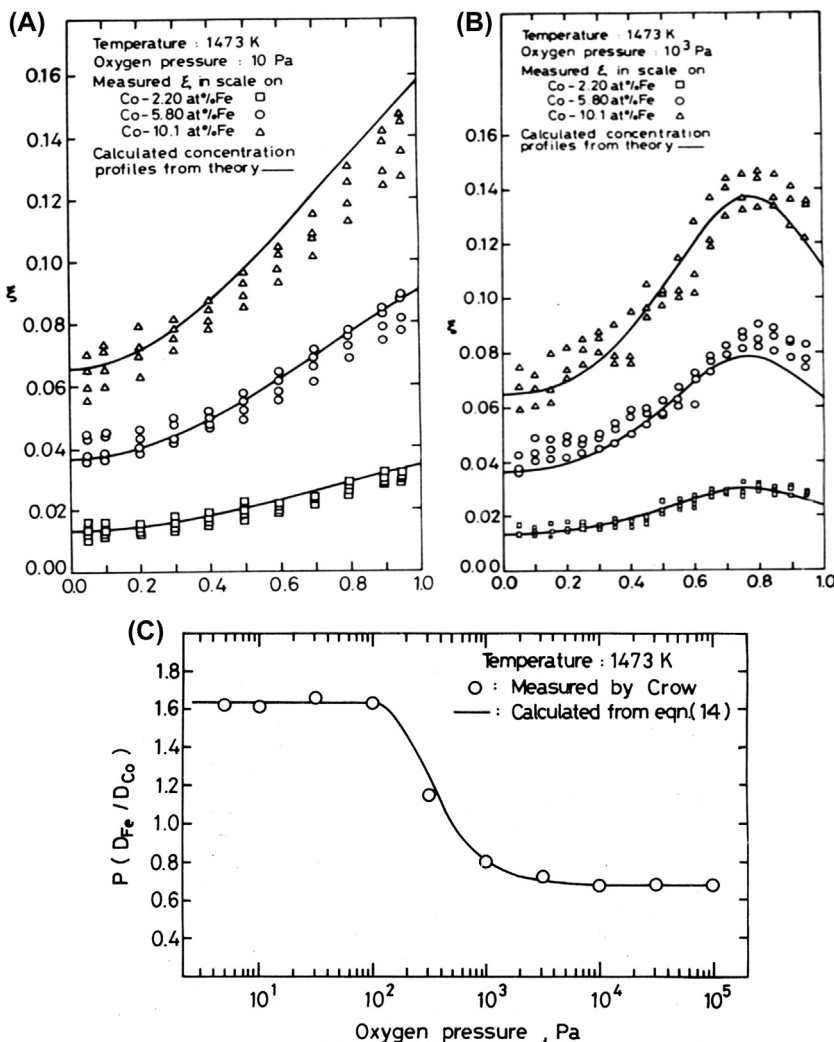


FIGURE 5.15 (A and B) Compositional profiles in (Co, Fe)O scales at low and high p_{O_2} values [36,37,41] (C) D_{Fe}/D_{Co} as a function of p_{O_2} [40]. Reproduced by permission of The Electrochemical Society.

through a decreased activation energy for diffusion or from an increase in defect concentration above that predicted for an ideal solution. The former possibility may be rejected on the basis of self-diffusion data [43–46] for $Fe_{1-\delta}S$ and $Ni_{1-\delta}S$. The latter possibility is supported by the concentration profiles in Fig. 5.16 as is now discussed.

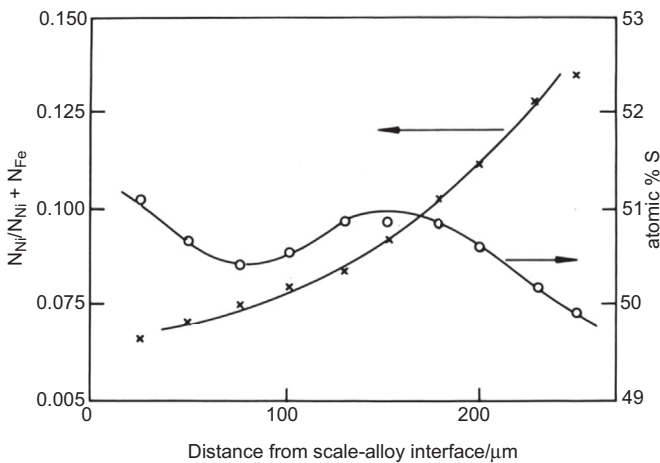


FIGURE 5.16 Compositional profiles in $(\text{Fe}, \text{Ni})_{1-\delta}\text{S}$ scale grown on Fe-41Ni at $T = 665^\circ\text{C}$ [37]. Reproduced by permission of The Electrochemical Society.

Recognising that the deviation from stoichiometry is given by

$$\delta = 1 - \frac{N_M}{N_S} \quad [5.81]$$

it is clear that δ varies with position in an unusual fashion in the $(\text{Fe}, \text{Ni})_{1-\delta}\text{S}$ scale. The values of δ calculated in this way range up to 0.04, much greater than the value of 0.02 reported [47] for $\text{Fe}_{1-\delta}\text{S}$ under these conditions. Since $\text{Ni}_{1-\delta}\text{S}$ has a smaller deviation from stoichiometry than $\text{Fe}_{1-\delta}\text{S}$, it is obvious that the solution is not ideal with respect to the defect species and, equivalently, to sulphur. The conclusion that a ternary solid solution may be close to ideal with respect to its component binary compounds but deviate strongly from ideality for the electronegative species is a common one.

If it is assumed that the pseudobinary solution FeS-NiS is ideal, that deviations from stoichiometry can be ignored and that $p = D_{\text{Fe}}/D_{\text{Ni}}$ is constant, independent of composition and a_s , then Eq. [5.67] can be rewritten as

$$(1-p) \frac{d\xi}{dy} + (1 - \xi + p\xi) \frac{d \ln a_s}{dy} = \frac{kp}{D_{\text{Fe}}} \quad [5.82]$$

If it is further assumed that the relationship between D_{Fe} and N_V (or δ) in the $(\text{Fe}, \text{Ni})_{1-\delta}\text{S}$ scale is the same as that given by Condit et al. [43] for $\text{Fe}_{1-\delta}\text{S}$

$$D_{\text{Fe}} = D_o \delta \exp \left[-(81 + 84\delta \text{ kJ mol}^{-1}) / RT \right] \quad [5.83]$$

then Eq. [5.82] can be applied to the data in Fig. 5.16 for ξ and δ as functions of y . This procedure permits the evaluation of the gradient $d \ln a_s/dy$, and p can then be varied to match the sulphur activity profile to the boundary values. The results of this calculation are shown in Fig. 5.17, where it is seen that

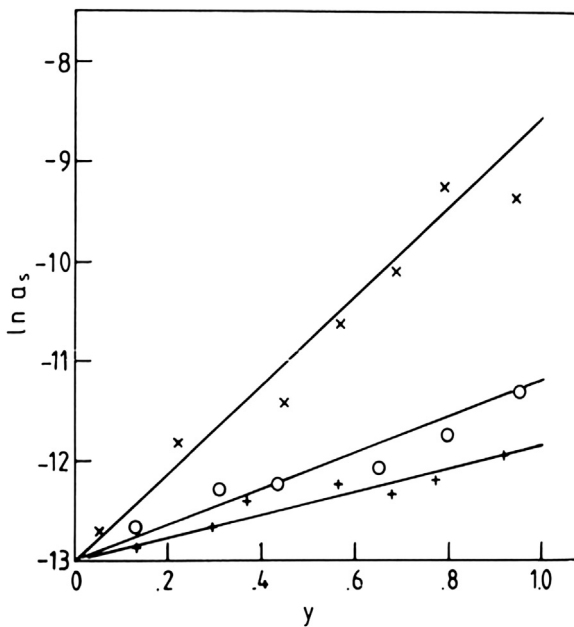


FIGURE 5.17 Sulphur activity profile in $(\text{Fe}, \text{Ni})_{1-\delta}\text{S}$ scale ($y = x/X$) calculated from Eqs [5.82] and [5.83] [37]. Reproduced by permission of The Electrochemical Society.

$d\ln a_s/dy$ is constant throughout the scale, despite the unusual behaviour of N_S . The value found for p was 0.4, consistent with the observed enrichment of nickel toward the scale surface.

The methods of calculating solid solution scale compositions and growth rates are complex and require a great deal of information on the thermodynamic and kinetic properties of the oxide. It is therefore much easier to measure scaling rates than it is to model them. Nonetheless, the experimental validation of the scaling theory has led to useful conclusions.

The growth of single-phase, solid solution scale layers is controlled by diffusion, and parabolic kinetics result. Scale compositions vary with position within the scale but are time invariant during steady-state reaction. The average scale composition is related to the ability of an alloy to deliver metal by diffusion to the scale-alloy surface. A useful form of this relationship has been provided by Bastow et al. [42].

$$\xi_{AV} = \int_0^1 \xi dy = \frac{N_B^{(o)} - N_{B,i}}{F(u)} + N_{B,i} \quad [5.84]$$

where $F(u)$ is as defined in Eq. [5.29] and, as before,

$$u = (k_c/2D_{AB})^{\frac{1}{2}} \quad [5.85]$$

If scaling is much faster than alloy diffusion, the situation for the MO and MS scales examined so far, then $N_{B,i} \approx N_B^{(o)}$ and the scale has the same average metal ratio as the alloy. If the reacting system is not at steady state, then $N_{B,i}$ changes with time, as must therefore ξ_{AV} . If an alloy becomes depleted in one component, then the other component will become enriched in the scale. If that component is the faster diffusing one, then its further enrichment at the scale surface may lead to the formation of a new oxide phase. The subsequently changed oxide constitution and morphology can be associated with loss of protective behaviour, as is discussed in [Section 5.9](#) and Chapter 7.

5.7 TRANSIENT OXIDATION

The discussion so far has been focused on the growth of an external scale under steady-state conditions. However, the time taken to achieve this steady state could be lengthy, in which case considerable scale would accumulate. The situation where only one oxide is stable was considered in [Section 5.4](#), where we concluded that the scale-alloy boundary conditions (and therefore the scaling rate) changed with time only if the kinetics were nonparabolic. Gesmundo et al. [48,49] have investigated this situation further, noting that a more realistic description of the early stage transient kinetics should involve a contribution to rate control by the scale-gas interaction processes. Thus scaling kinetics are expected to show a transition from an initial linear form to subsequent parabolic behaviour as the scale thickens and eventually diffusion becomes slower than the scale-gas interfacial process. It was shown that under these conditions the value of $N_{B,i}$ decreased monotonically from $N_B^{(o)}$ to the steady-state value, with no minimum of the sort suggested by Whittle et al. [14]. The different conclusions were consequences of the different kinetic models used for the transient stage.

The consequences of the transient oxidation stage are potentially more significant in the case where more than one oxide can form, and the oxides have limited intersolubility. An example is provided by the oxidation of binary Cu-Zn alloys, studied long ago by Dunn [50] and subsequently by others.

Relative oxidation rates of these alloys are indicated by the data in [Fig. 5.18](#). Alloys containing up to 10% Zn react at 800°C according to parabolic kinetics at essentially the same rate as pure copper, producing a Cu₂O scale with inclusions of ZnO [51]. If the alloy zinc level is $\geq 20\%$, the oxidation rate is orders of magnitude less, independent of $N_{Zn}^{(o)}$, and corresponds to the growth mainly of the more stable ZnO. Wagner [12] calculated the value of $N_{Zn,min}$ from [Eq. \[5.25\]](#), modified to take into account the variation of D_{Zn} with composition [52]. The resulting values for $N_{Zn,min}$ of 0.14, 0.15 and 0.16 at 725, 800 and 800°C are in reasonably good agreement with experimental observation ([Fig. 5.18](#)). Alloys containing intermediate zinc levels of 10–20% showed wide deviations from parabolic kinetics [53], as

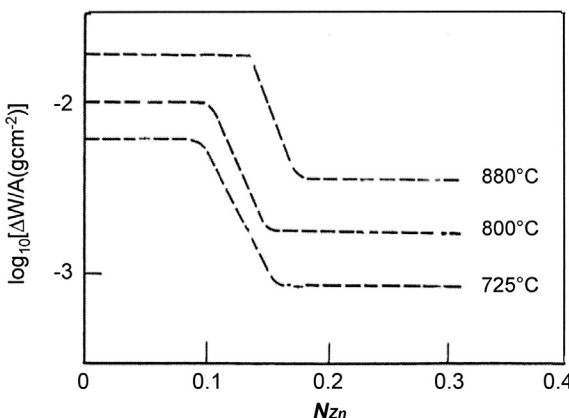
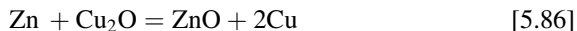


FIGURE 5.18 Oxidation of Cu-Zn alloys: weight uptake after five-hour reaction at $p_{O_2} = 1$ atm [51]. With permission of TMS.

seen in Fig. 5.19. The rate was initially similar to that of pure copper, but subsequently decreased significantly as a ZnO layer developed at the base of the scale. If the reaction was interrupted by a one-hour anneal under argon, the ZnO layer developed during this time. When oxidation was resumed, slow parabolic kinetics were observed, and the rate was characteristic of high zinc content alloys.

This pattern of behaviour can be understood in terms of an initial, transient reaction period during which both Cu₂O and ZnO nucleate on the surface [54,55]. The faster growing Cu₂O overgrows the ZnO, which remains as slow-growing particles at the scale-alloy interface (Fig. 5.20). During this stage, the overall scaling kinetics are similar to those of single-phase Cu₂O layer growth, since this phase constitutes the majority of the scale. This initial stage of preferential copper oxidation leads to zinc enrichment at the alloy-scale interface, and the reaction



commences. This process is thermodynamically favoured, with $\Delta G^\circ = -164 \text{ kJ mol}^{-1}$ at 800°C, corresponding to

$$\frac{a_{\text{Cu}}^2}{a_{\text{Zn}}} = 9.6 \times 10^7 \quad [5.87]$$

Thus, at local equilibrium, $a_{\text{Zn}} \approx 10^{-8}$, and the transient formation of Cu₂O is a consequence of the reaction kinetics. Whereas Cu₂O growth is rapid, the displacement reaction Eq. [5.86] is slow. Eventually, however, the displacement reaction becomes kinetically favoured, and the alloy surface area fraction covered with ZnO increases to unity, as shown schematically in Fig. 5.20. Once coverage with ZnO is complete, further Cu₂O growth ceases because

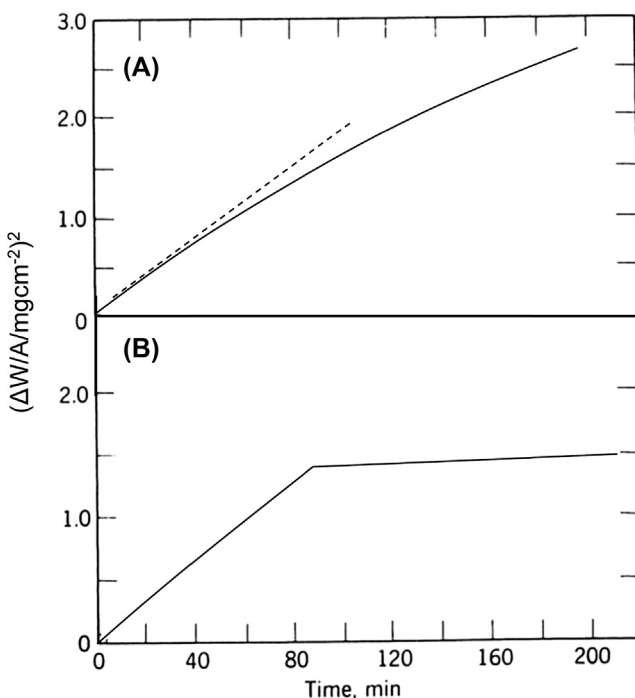


FIGURE 5.19 Oxidation kinetics observed for Cu-15 Zn at $T = 700^\circ\text{C}$, and $p_{\text{O}_2} = 1 \text{ atm}$: (A) continuous and (B) interrupted by one-hour anneal in Ar [53]. Reproduced by permission of The Electrochemical Society.

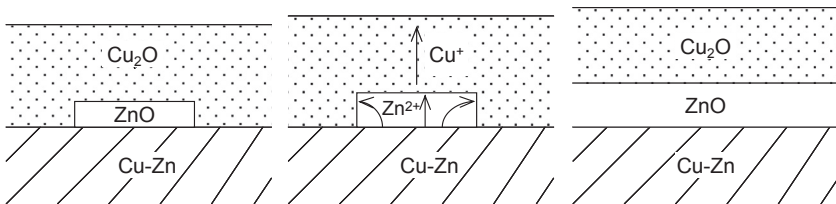
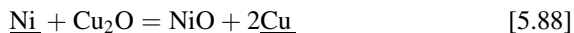


FIGURE 5.20 Schematic view of transient Cu₂O overgrowing ZnO and eventually being isolated from Cu-Zn alloy as the ZnO layer becomes complete.

copper is essentially insoluble in the zinc oxide. Further scale growth then consists of ZnO layer thickening under steady-state diffusion control.

Wagner [12] carried out a similar analysis for the oxidation behaviour of Cu-Ni alloys. Using Eq. [5.25], he calculated that for exclusive NiO formation a value of $N_{\text{Ni},\text{min}} = 0.75$ was required at 950°C . This was in satisfactory agreement with the change in alloy oxidation rate observed by Pilling and Bedworth [56] at a value of about 0.7. However, scaling rates in the range

$0.7 < N_{\text{Ni}}^{(o)} < 1$ were greater than for pure nickel, increasing with the level of copper. As with the Cu-Zn system, the high diffusion coefficient of Cu_2O meant that regions of this oxide remaining from the initial transient stage of oxidation continued to grow fast. Evidently the displacement reaction



is slow, and regions of Cu_2O persist at the scale-alloy interface for long times [53,57]. It may be that nucleation of new NiO regions at the $\text{Cu}_2\text{O}/\text{alloy}$ interface is energetically unfavourable, and that the lateral spreading of original surface NiO nuclei is also slow.

Transient oxidation processes occurring prior to the establishment of steady-state protective scales of Cr_2O_3 or Al_2O_3 are rather different from the Cu-Zn and Cu-Ni systems described above. The much greater stability of chromia and alumina makes internal precipitation of these oxides more likely. The discussion is therefore postponed until internal oxidation processes are considered in Chapter 6.

Even when only one metal is oxidised, nonsteady-state oxidation can take place in an initial transient period associated with phase transformations in the oxide. The technologically important example of alumina scale formation is now considered.

5.7.1 Transient Behaviour Associated With Alumina Phase Transformations

Alumina exists in a number of crystalline forms, only one of which, the hexagonal α -phase, is thermodynamically stable [58]. However, the other phases retain their crystalline forms indefinitely below certain temperature limits [58], as shown approximately in Fig. 5.21. The long-term existence of these metastable phases arises from the difficulty of achieving the transformations through which the material must pass to reach the stable α -phase. Activation barriers may, of course, be overcome thermally, but the magnitude of the barriers may also be altered by the presence of foreign phases, either gaseous or solid [59,60], and by dissolved impurity species [61]. As seen in

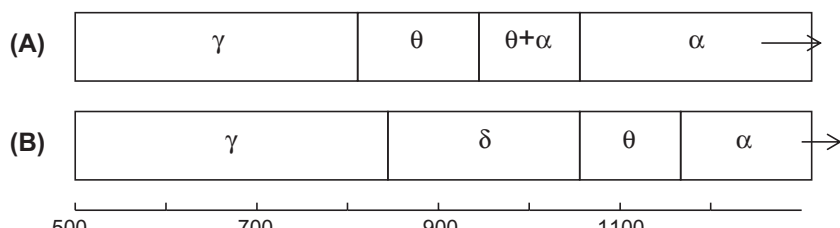


FIGURE 5.21 Approximate Al_2O_3 transformation temperatures observed [58] on bulk material used for catalyst supports. (A) $\gamma\text{-Al}_2\text{O}_3+3\%\text{Pt}$ (B) $\gamma\text{-Al}_2\text{O}_3$. Reproduced with the permission of The American Ceramic Society.

Fig. 5.21, the presence of platinum in contact (as a dispersed catalyst) with $\gamma\text{-Al}_2\text{O}_3$ alters the sequence of its phase transformations and generally lowers the temperatures at which they occur. Nickel has also been shown [62] to accelerate transformation to $\alpha\text{-Al}_2\text{O}_3$ at temperatures of 850 and 950°C. As discussed later in this section, chromium and iron also affect the transformation.

Oxidation of alumina-forming alloys at temperatures below about 1200°C often leads initially to the formation of transient, metastable alumina scales [63–88]. This is significant, because the metastable aluminas grow much more rapidly than $\alpha\text{-Al}_2\text{O}_3$ [63–88]. A comparison of scaling rates for θ and $\alpha\text{-Al}_2\text{O}_3$ in **Fig. 5.22** illustrates this point. An example of the transition from fast transient oxidation to slow, steady-state $\alpha\text{-Al}_2\text{O}_3$ growth observed by Rybicki and Smialek [64] for the intermetallic $\beta\text{-NiAl}$ containing 0.05 a/o Zr is shown in **Fig. 5.23**.

The metastable aluminas have lower densities than $\alpha\text{-Al}_2\text{O}_3$, and transformation is accompanied by a 13% reduction in volume. The higher growth rates of the metastable oxides are related to their different crystal structures ($\gamma\text{-Al}_2\text{O}_3$ has a cubic spinel type structure [66], the structure of $\delta\text{-Al}_2\text{O}_3$ is the subject of some disagreement [67] and $\theta\text{-Al}_2\text{O}_3$ is monoclinic) and looser packing than the $\alpha\text{-Al}_2\text{O}_3$ structure of hexagonal close-packed oxygen with aluminium occupying octahedral interstitial sites. The different morphologies developed by the alumina phases also contribute to their differing growth rates: whereas $\alpha\text{-Al}_2\text{O}_3$ is a dense layer, the metastable forms tend to develop as blades and whiskers.

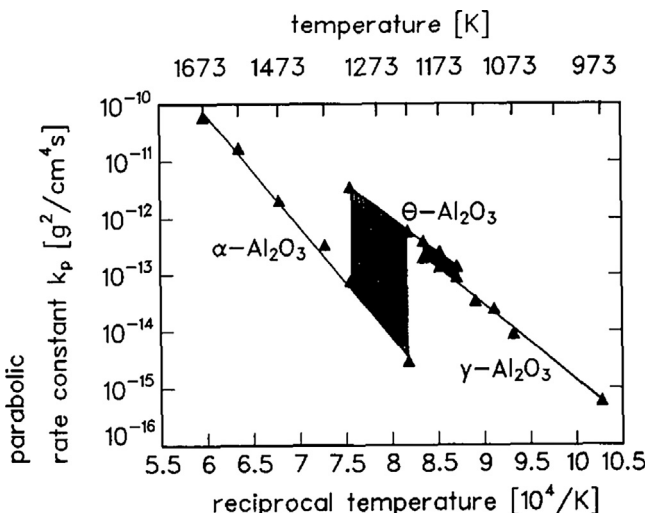


FIGURE 5.22 Rates of θ -, γ - and $\alpha\text{-Al}_2\text{O}_3$ scale growth on $\beta\text{-NiAl} + \text{Zr}$ [65]. Reprinted from M.W. Brumm, H.J. Grabke, Corros. Sci. 33 (1992) 1677, with permission from Elsevier.

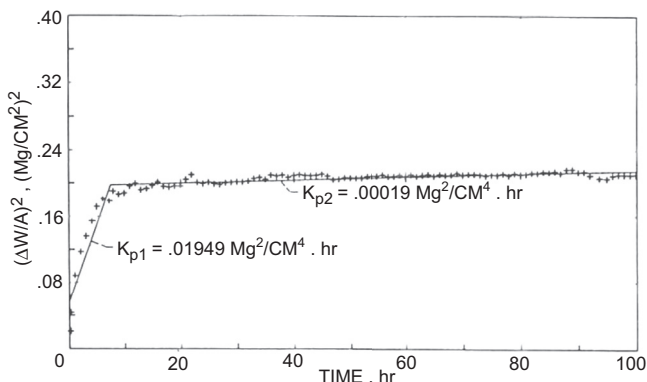


FIGURE 5.23 Transition from fast transient oxidation to steady-state α - Al_2O_3 growth on β -NiAl + Zr [64]. With kind permission from Springer Science and Business Media.

Considerable information is available for the oxidation of the intermetallic β -NiAl. This material has good oxidation resistance due to its ability to form scales which are exclusively Al_2O_3 [15]. It has been studied intensively because it is the principal constituent of diffusion coatings grown on nickel-base superalloys to provide protection against oxidation.

The transient oxide grown on β -NiAl + Zr at 900°C was found to have a blade or platelet structure and was identified by XRD as θ - Al_2O_3 . At 800 and 900°C, the first formed oxide was γ - Al_2O_3 but was replaced by θ - Al_2O_3 after about one hour [68]. At these temperatures, the θ -phase persisted for at least 100 h. At 1000 and 1100°C, however, the θ -phase was replaced by α - Al_2O_3 , which nucleated in the prior θ - Al_2O_3 scale. These nuclei grew laterally, until they impinged to form grain boundaries [68,69], the transformation to α - Al_2O_3 then complete. Shrinkage cracks within the grains resulted from the volume change accompanying the θ - α transformation. The grain boundaries formed where the α - Al_2O_3 islands met provided pathways for rapid diffusion, leading to the development of oxide ridges, as proposed by Hindam and Smeltzer [20]. Plan and cross-sectional views of the ridge structure are shown in Fig. 5.24. The ridges remain on the surface but do not continue to grow in proportion to the underlying scale thickness.

The nucleation sites for α - Al_2O_3 formation are of interest. On the basis of their TEM observations, Doychak et al. [69] suggested that nucleation commenced preferentially at the oxide-gas surface. Smialek and Gibala [71] concluded that the transient oxidation of Ni-Cr-Al alloys was ended by nucleation of α - Al_2O_3 at the scale-alloy interface. Both of these investigations relied upon TEM examination in which the electron beam was transmitted through the scale thickness, and the location of the α -nuclei was therefore ambiguous. Subsequent observations [72] of fracture sections of

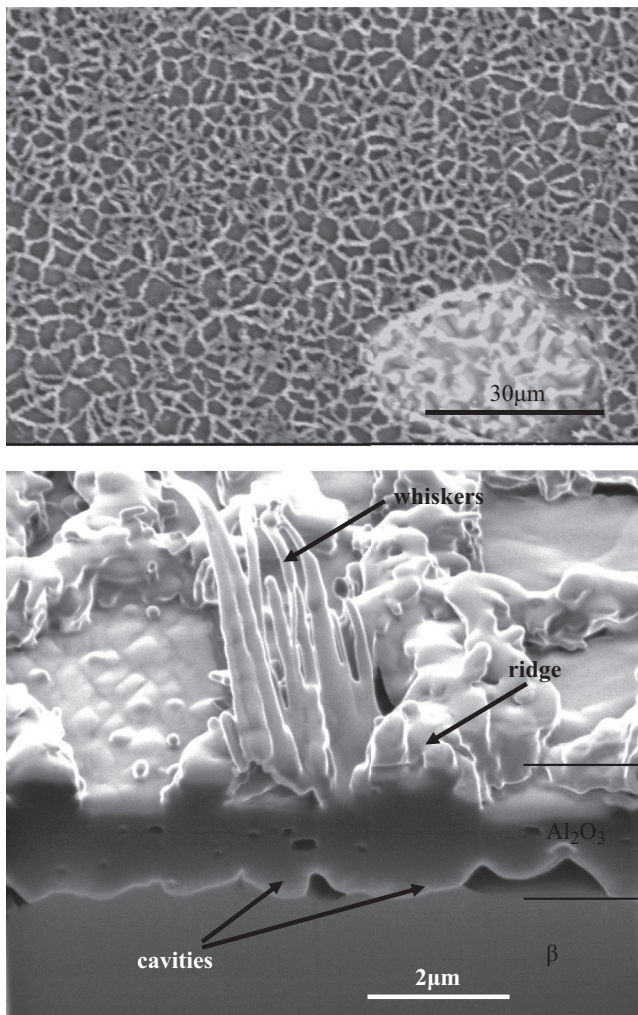


FIGURE 5.24 Ridges of $\alpha\text{-Al}_2\text{O}_3$ developed on $\beta\text{-NiAl}$ where islands of $\alpha\text{-Al}_2\text{O}_3$ had met: upper: SEM plan and lower: FIB cross-section views. Localised spallation visible in plan view [70]. Reproduced by permission of The Electrochemical Society.

scales grown on $\beta\text{-NiAl}$, reproduced in Fig. 5.25, show that the α -phase grew at the metal-scale interface.

Minor alloy additions to the $\beta\text{-NiAl}$ can affect the rate at which steady-state $\alpha\text{-Al}_2\text{O}_3$ growth is achieved. Both zirconium and ion-implanted yttrium slow the transformation from θ to $\alpha\text{-Al}_2\text{O}_3$ [73,74]. Fine oxide dispersions in the alloy can also affect the transformation. Pint et al. [75] showed that dispersed Y_2O_3 , ZrO_2 , La_2O_3 and HfO_2 all delayed slightly the θ -to $\alpha\text{-Al}_2\text{O}_3$ transformation during initial oxidation of $\beta\text{-NiAl}$ at 1000°C . On the

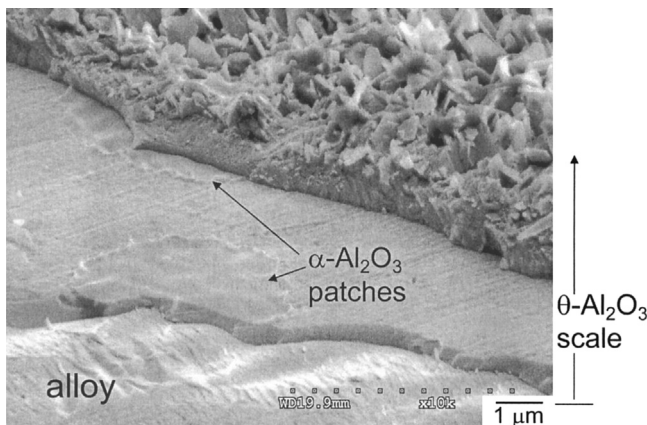


FIGURE 5.25 SEM view of fracture section of alumina scale grown at 1100°C on β -NiAl, showing α -grains at the scale-alloy interface [72]. Published with permission from *Science Reviews*.

other hand, dispersions of α - Al_2O_3 and TiO_2 both accelerated the transformation. The delays caused by Y, Zr, La and Hf oxides were attributed to the effect of dissolution into the transient oxide. According to Burtin et al. [61], larger ions inhibit the θ to α transformation. It was suggested that such dopants could interfere with both the surface area reduction and the diffusionless transformations required to convert θ - Al_2O_3 blades to dense α - Al_2O_3 . The accelerating effect of α - Al_2O_3 inclusions was presumably simply one of nucleation. Alloy additions of chromium can also accelerate the transformation through initial formation of Cr_2O_3 which, being isotypic with α - Al_2O_3 , promotes its nucleation [76].

Ferritic FeCrAl alloys such as Kanthal (Table 5.1) are also alumina formers. At temperatures of 1000°C and higher, the α -phase is quickly formed, providing good protection. This is thought to be due to transient formation of Fe_2O_3 , which is also structurally isotypic with α - Al_2O_3 , and promotes its nucleation. Confirmation of this has been provided by N'Dah et al. [77], who oxidised commercial FeCrAl alloys in Ar-H₂-H₂O atmospheres at 1100 and 1200°C. If the H₂O(g) level was high enough to yield a p_{O_2} value above the $\text{Fe}_2\text{O}_3/\text{FeAl}_2\text{O}_4/\text{Al}_2\text{O}_3$ equilibrium value, a scale of 100% α - Al_2O_3 was obtained. However, if the water vapour level was lower, a mixture of α - and θ - Al_2O_3 resulted.

At lower temperatures, the scales formed on FeCrAl alloys can contain metastable aluminas and consequently can provide poor protection [78–80]. A TEM cross-sectional view [81] of the scale grown on Kanthal AF (Table 5.1) at 900°C in an atmosphere of O₂ + 40% H₂O is shown in Fig. 5.26. An EDAX line scan across the scale revealed a narrow central region rich in chromium. This was a residue of the initial stage of transient oxidation in which Fe, Cr

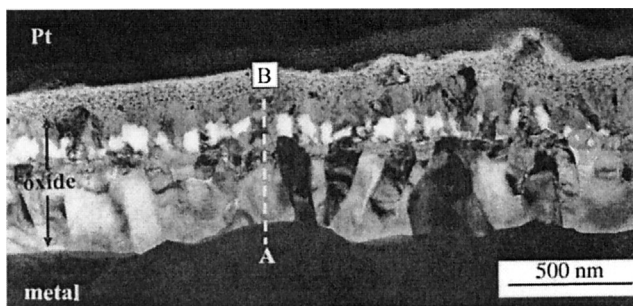


FIGURE 5.26 TEM cross-sectional view of scale grown on Kanthal AF at 900°C [81]. Bright material in middle of scale is chromium-rich remnant from transient oxidation. *Published with permission from Science Reviews.*

and Al all oxidised. The iron had subsequently diffused into the outer scale region, where oxygen activities were higher. The outer layer was $\gamma\text{-Al}_2\text{O}_3$ whereas the inner layer was $\alpha\text{-Al}_2\text{O}_3$. The latter had nucleated at the chromium-rich region and grown inwards and laterally to form a protective layer. Before that layer was complete, the outer $\gamma\text{-Al}_2\text{O}_3$ layer developed. Its stability was thought to be enhanced by the presence of water vapour. An increase in the amount of transient oxidation of a variety of alumina-forming alloys when exposed to humid air has also been reported by Maris-Sida et al. [82].

The more rapid growth of transient metastable aluminas can cause more severe depletion of the alloy aluminium. Pragnell et al. [83] studied the oxidation of commercial FeCrAl foils of nominal thickness 50 μm at 900°C. They observed rapid initial growth of transient $\theta\text{-Al}_2\text{O}_3$, which was transformed only slowly to $\alpha\text{-Al}_2\text{O}_3$. The total weight uptake after 72 h was $\sim 0.4 \text{ mg cm}^{-2}$, much more than that corresponding to protective $\alpha\text{-Al}_2\text{O}_3$ scale growth. Measurements of alloy aluminium concentrations (Fig. 5.27) show that the depletion levels were consequently significant.

A strongly beneficial effect of titanium in promoting $\alpha\text{-Al}_2\text{O}_3$ formation has been reported. As noted earlier, dispersed TiO_2 in $\beta\text{-NiAl}$ accelerated transformation of transient alumina to the α -phase. Comparisons [84] of the oxidation kinetics of different FeCrAl grades at 850–925°C have shown that Kanthal AF reached steady-state $\alpha\text{-Al}_2\text{O}_3$ growth the fastest. This grade contains nominally 0.1% Ti. Prasanna et al. [85] showed that titanium from the alloy was incorporated into the oxide scale, possibly accelerating the $\theta\text{-}\alpha$ transformation. The application of a slurry of TiO_2 to the FeCrAl surface prior to oxidation has also been shown [81,86] to accelerate $\alpha\text{-Al}_2\text{O}_3$ formation. Since TiO_2 was used by one set of investigators [81] in the form of rutile and by the other [86] as anatase, it seems that the chemical rather than the structural nature of TiO_2 was important. Finally, oxidation of $\gamma\text{-TiAl}$ alloys

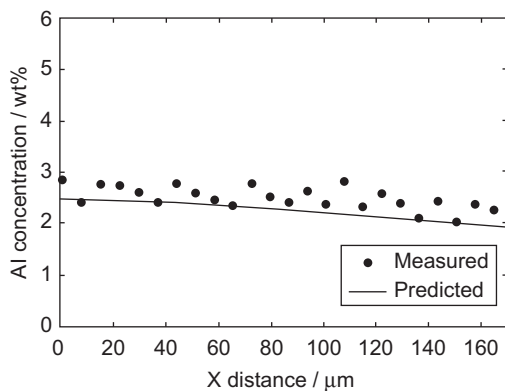


FIGURE 5.27 Aluminium depletion caused by rapid transient oxidation of FeCrAl at 900°C [83]. Published with permission from *Science Reviews*.

produces α - Al_2O_3 along with TiO_2 at temperatures where other alumina formers develop transient oxides [87]. Pint et al. [75] have suggested that the accelerating effect of titanium is consistent with the findings of Burtin et al. [61] in that the Ti^{4+} ion is of similar size to Mg^{2+} , which has been found also to be a phase change accelerator.

It seems that the transient behaviour of alumina scales is affected by a large number of variables, and that information is still being collected (see Section 5.10.1). Nonetheless, it also seems that ways of accelerating the phase transformations, and thereby lessening the amount of transient oxidation, are being developed. Quantification of alumina transformation kinetics under various circumstances is highly desirable. Temperature-time-transformation plots, such as those in Fig. 5.28 due to Andoh et al. [88], provide a useful representation of such data.

5.8 MICROSTRUCTURAL CHANGES IN SUBSURFACE ALLOY REGIONS

As is by now clear, scale growth almost always leads to the development of compositional changes in the alloy subsurface as the result of the different rates at which alloy components are oxidised. The diffusion processes involved can lead to volume changes, breakdown in the morphological stability of the scale-alloy interface, depletion and dissolution of minority phases, precipitation of new phases and other transformations resulting from the compositional changes, as discussed below. The additional possibility of inward oxygen diffusion leading to internal oxide precipitation will be dealt with in Chapter 6.

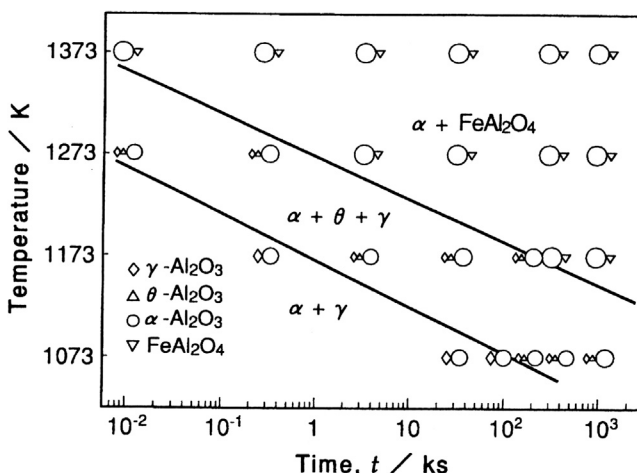


FIGURE 5.28 Temperature-time-transformation plots for alumina formed on Fe-20Cr-5Al [88]. Published with permission from Trans Tech Publications.

5.8.1 Subsurface Void Formation

An example of void formation within β -NiAl beneath an alumina scale is shown in Fig. 5.6. The alloy surface revealed by scale removal shows the voids to be faceted and of varying aspect ratios. The cross-sectional view shows that the Al_2O_3 undersurface is flat, as the void developed in the metallic phase. There are several possible ways in which such voids could form.

Growth of an external scale by outward metal transport means that new oxide is formed at the scale-gas interface and cannot in any direct sense fill the space vacated by the reacted metal. However, plastic deformation of the scale can allow it to retain contact with the retreating metal surface, if scale movement is unconstrained. To the extent that plastic deformation is not available, void space develops somewhere within or beneath the scale. In the case of a completely rigid scale, the total void volume would equal the volume of metal consumed by oxidation. The location of the voids depends on the detailed transport mechanisms in effect. In solid solution alloys, mass transport occurs via vacancy diffusion, and the origins and sinks for these defects must be considered.

It is assumed [89–91] that vacancies are injected at the scale-metal interface, as metal atoms move into the scale. If these are annihilated at dislocations, they cannot cause void formation within the metal, but nonetheless, the reacting metal shrinks. If, as is being supposed, the oxide scale is unable to conform with the shrinking metal core, void space must be generated elsewhere by the creation of new vacancies. These can be emitted from dislocations in the reverse of the annihilation process. Thus dislocations serve as very

rapid pathways for the transmission of vacancies and thereby of void space. Voids develop where vacancies can aggregate, ie, ‘coalesce’ or ‘condense’, in what must be a nucleation process. Preferred sites for void nucleation will therefore be phase interfaces and alloy grain boundaries. Moreover, the development of a vacancy concentration gradient from a maximum at the scale-alloy interface to a minimum in the alloy interior will lead to a greater number of voids nucleating immediately beneath the scale than deeper into the alloy. This was the experimental finding of Hales and Hill [89] in the case of pure nickel. Of course, the vacancy injection, transport and condensation model is applicable to both metals and alloys.

Alloys are subject to an additional effect, arising from the different mobilities of the constituent metals. Consider the case of β -NiAl forming an external scale of pure Al_2O_3 and voids at the alloy-scale interface [92–95]. Brumm and Grabke [96] have investigated void formation in a series of β -NiAl compositions within the homogeneity range of this phase (20 at. % at 1200°C). They found that void formation decreased with increasing alloy $N_{\text{Al}}/N_{\text{Ni}}$ ratio. This was explained using the diffusion data [97] shown in Fig. 5.29. As seen from the figure, $D_{\text{Ni}}/D_{\text{Al}} \approx 3$ for $N_{\text{Al}} \leq 0.5$. The selective oxidation of aluminium from β -NiAl necessarily depletes aluminium from the alloy surface and enriches nickel, as shown schematically in Fig. 5.3. In the case of nickel-rich alloys the high value of $D_{\text{Ni}}/D_{\text{Al}}$ means that the inward flux of nickel exceeds the outward flux of aluminium. Such a situation of unbalanced material flows is known as the Kirkendall effect and was analysed in Section 2.7. In that discussion, it was assumed that the lattice was free to move, and its resulting drift rate, v , reflected the different metal self-diffusion coefficients

$$v = V_{AB}(D_A - D_B)\nabla C_A \quad [5.89]$$

In the case of β -NiAl oxidation, however, the alloy surface is anchored to an almost rigid alumina scale and is not free to move. The vacancy flux induced by the imbalance between J_{Ni} and J_{Al} therefore leads to void formation rather than lattice drift. Evidently, void nucleation at the alloy-surface interface is energetically favoured over other sites within the bulk alloy. In aluminium-rich NiAl, however, diffusion of aluminium is the dominant process (Fig. 5.29), and the Kirkendall effect ceases to drive vacancies towards the alloy surface [98,99].

The voids continue to enlarge with time as NiAl oxidation proceeds, despite the gaps developed between alloy and oxide. At 1200°C, the vapour pressure of aluminium above the depleted alloy is sufficient to transport Al(g) across the cavity to the scale, sustaining its continued growth [22,96]. At temperatures below 1000°C, the value of p_{Al} is too low, according to (Eq. [2.155]), to maintain the observed oxide scaling rate. Some other transport mechanism, perhaps surface diffusion, must be involved [96].

The development of the interfacial voids obviously weakens scale adhesion, making scale loss more likely. Platinum is added to NiAl to improve its

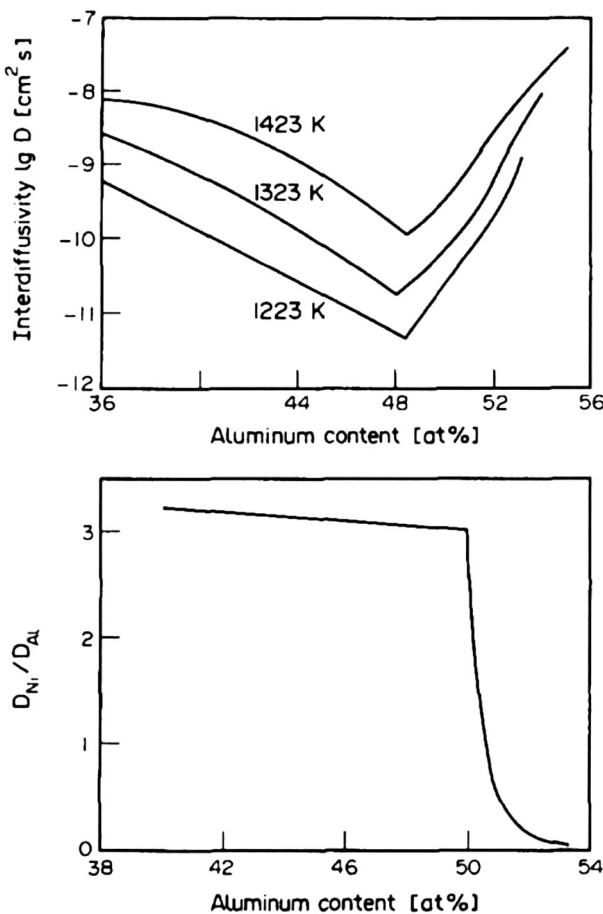


FIGURE 5.29 Interdiffusion and self-diffusion coefficients in β -NiAl [97]. Reprinted from M.W. Brumm, H.J. Grabke, Corros. Sci. 34 (1993) 547, with permission from Elsevier.

scale adherence [100]. The improvement is associated with a reduction in cavity formation [101], an effect thought to result from interactions within the alloy increasing D_{Al} and/or decreasing D_{Ni} . Gleeson et al. [102] have confirmed that platinum increases D_{Al} in β -NiAl.

A completely different mechanism of void formation is available in cases where the alloy contains carbon. Inward diffusing oxygen can react with solute carbon to form bubbles of CO_2 , as has been shown experimentally [103–105]. Fracture of oxidised specimens in a vacuum chamber attached to a mass spectrometer revealed the presence of CO_2 . The extent of void formation was shown to increase with carbon content and could be suppressed by decarbonisation prior to oxidation. This mechanism can operate in both alloys and single metals.

5.8.2 Scale-Alloy Interface Stability

The additional degree of freedom available in a binary alloy plus oxygen system permits the development of a two-phase region in a diffusion zone, unlike the case of pure metal oxidation, where such zones are thermodynamically impossible in the absence of capillarity effects. For this reason, pure metal-scale interfaces are stable. However, no such thermodynamic constraint applies to alloy-scale interfaces, the shapes of which are kinetically controlled. An example of an unstable interface is shown in Fig. 5.1A. The general nature of the problem is rather simple, as shown in Fig. 5.30, where a perturbation in an otherwise flat alloy-scale interface is represented. If such a perturbation grows, the interface is unstable; if it decays, the interface is stable.

The effect of the perturbation is locally to decrease the scale thickness from X to X' and increase the alloy depletion depth from X_D to X'_D . Clearly, if scale

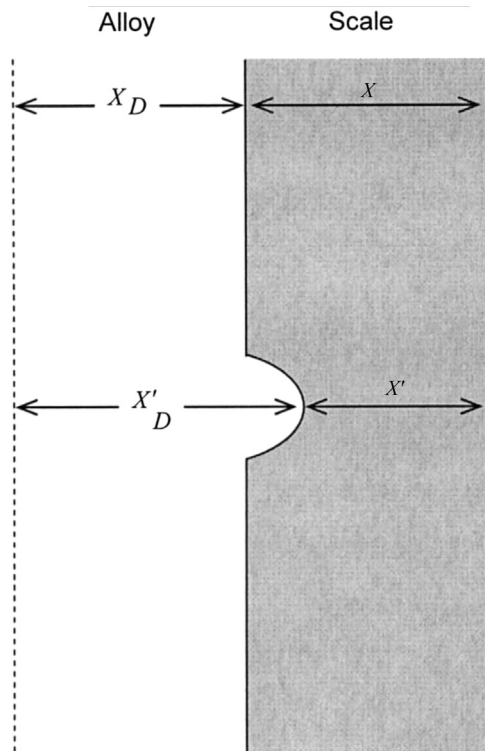


FIGURE 5.30 Schematic view of growth and decay of perturbation at alloy-scale interface, according to which phase is the slower diffusing.

growth is controlled by scale diffusion, ie, $dX/dt = k_p/X$, then growth is faster at the site of the perturbation. Accordingly, metal is consumed faster at this site than on the flat surface, a process which continues until a uniform scale thickness is restored. It is seen that the interface is stable when scale diffusion is rate controlling. Consider now the situation where alloy diffusion is rate controlling, and to a first approximation, the flux of B is proportional to \tilde{D}_{AB}/X_D . Clearly this flux is slowest at the site of the perturbation, shown in Fig. 5.30, because $X'_D > X_D$. Thus oxidation of the flat part of the interface is faster than at the perturbation, causing the flat surface to recede faster than the locally perturbed region. In this case, the irregularity grows and the interface is unstable.

The conditions under which diffusion in the alloy controls scaling rates were examined by Wagner [12], as discussed in Section 5.3. Wagner [106] extended that analysis to consider the possibility of morphological breakdown, assuming that no oxygen dissolved in the alloy and that surface capillarity effects can be neglected. He found from a two-dimensional analysis of diffusion at a sinusoidal scale-alloy interface that the condition for interface stability is

$$\frac{N_{B,i}}{1 - N_{B,i}} \frac{D_{AB}}{D_B} \frac{V_{OX}}{V_{AB}} > 1 \quad [5.90]$$

where now $N_{B,i}$ represents alloy composition at the average interface location. When, on the other hand, the interface is unstable, it is likely that particles of the more noble metal will be occluded into the oxide. Whittle et al. [107] have examined the effect of relaxing the assumptions of negligible oxygen solubility in the alloy and of the more noble metal in the oxide. They found that internal precipitation of BO behind the alloy-scale interface was a likely outcome under the supposed conditions.

5.8.3 Phase Dissolution

The situation considered is that of a two-phase alloy in which a precipitate phase rich in the more reactive solute element acts as a reservoir for the continued exclusive growth of the solute metal oxide scale. A schematic representation is shown in Fig. 5.31, using the example of a Ni-Si alloy. The concentration profile of reactive metal B is defined by the original alloy mole fraction $N_B^{(o)}$, the solubility limit in the matrix phase, N_B^a , and the alloy-scale boundary value. It is assumed that precipitate dissolution is fast enough to maintain local precipitate-matrix equilibrium. If diffusion of B through the solute-depleted subsurface alloy region is also fast enough, then $N_{B,i}$ will be approximately constant, and steady-state parabolic kinetics result. Diffusion analysis [108] yields the concentration profile of B in the single-phase

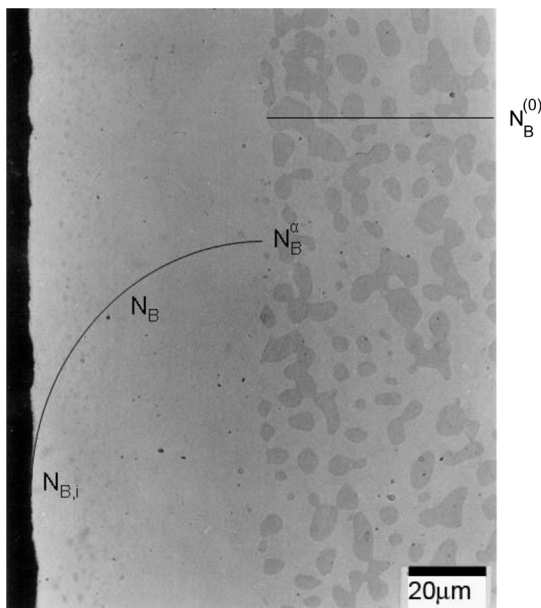


FIGURE 5.31 Selective oxidation of two-phase alloy AB causing dissolution of B -rich phase and diffusion through depletion zone.

dissolution zone. Approximating the scale-alloy interface as immobile, one finds from a mass balance for B that

$$N_B^{(o)} - N_{B,i} = \frac{u}{\gamma \exp(\gamma^2)} + \pi^{\frac{1}{2}} u \operatorname{erf}(\gamma) \quad [5.91]$$

where

$$u = (k_c / 4\tilde{D}_{AB})^{\frac{1}{2}} \quad [5.92]$$

$$\gamma = (X_d / 4\tilde{D}_{AB}t)^{\frac{1}{2}} \quad [5.93]$$

and X_d represents the precipitate dissolution depth. A slightly more accurate description is obtained by taking scale-metal interface movement into account [108]. Application of Eq. [5.91] to the kinetics of precipitate dissolution zone widening during oxidation of Ni-Si alloys consisting of a γ -matrix and β -Ni₃Si precipitates and of Co-Si alloys containing α -Co₂Si precipitate led to successful prediction [109] of depletion depths (Fig. 5.32).

Two questions arise when considering the selective oxidation of protective scale-forming metals from two-phase alloys. Firstly, will the precipitates dissolve fast enough to maintain the solute level at its equilibrium value N_B^α ? Secondly, will diffusion through the depleted zone be fast enough to maintain

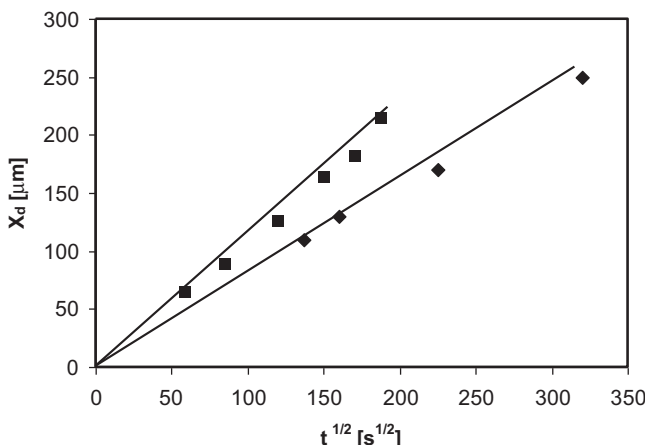


FIGURE 5.32 Depletion zone deepening kinetics for Ni-16Si ■ and Co-19Si ♦. Continuous lines predicted from Eq. [5.91]. Reprinted from D.J. Young, B. Gleeson, Corros. Sci. 44 (2002) 345, with permission from Elsevier.

$N_{B,i}$ at a high enough level to sustain selective scale growth? The second problem is similar to the situation of diffusion from a single-phase alloy considered by Wagner [12] and discussed here in Section 5.3. In both cases, diffusion through a single-phase, subsurface alloy zone delivers B to the scale-alloy interface, and the ratio k_c/\tilde{D}_{AB} is a key factor. This has been demonstrated [110] by comparing austenitic and ferritic modifications of a series of cast iron-chromium carbide alloys.

The software package THERMO-CALC [111] was used to predict how alloying additions would affect the phase constitution and to calculate alloy and precipitate compositions and weight fractions. The base alloy chosen for investigation was Fe-15Cr-0.5C at 850°C, where it is austenitic. Alloy compositions are listed in Table 5.4 along with their predicted phase constitutions. Matrix chromium contents were around 11 wt.% and the coarse interdendritic carbides varied in volume fraction from 6% to 10%.

Adding silicon to the iron-base alloy altered its phase constitution to $\alpha + M_7C_3$. In order to study the chemical effect of silicon in isolation from its effect on the matrix crystal structure, another alloy was designed to retain the austenite structure by using nickel as an austenite stabiliser. To complete the iron-based alloy set, an $\alpha +$ carbide steel was produced to investigate the effect of changing matrix to ferrite without simultaneously introducing silicon. Molybdenum was chosen as the ferrite stabiliser. To verify that the molybdenum had no major effect other than producing a ferrite matrix, a molybdenum-bearing austenitic alloy was designed, again using nickel as the austenite stabiliser.

TABLE 5.4 Oxidation of Cast Ferrous Alloys in Oxygen at 850°C

Composition (wt.%)	Phase Constitution	Reaction Morphology	$k_p(\text{g}^2 \text{cm}^{-4} \text{s}^{-1})$
Fe-15Cr-0.5C	$\gamma + M_{23}C_6$	Iron oxide scale Carbides engulfed	2.5×10^{-8}
Fe-15Cr-0.5C-3Mo	$\alpha + M_{23}C_6$	Cr_2O_3 scale Carbide dissolution zone	1.4×10^{-11}
Fe-15Cr-0.5C-3Mo-3Ni	$\gamma + M_{23}C_6$	Iron oxide scale Carbides engulfed	9.3×10^{-9}
Fe-15Cr-0.5C-1Si	$\alpha + M_7C_3$	Cr_2O_3 scale Carbide dissolution zone	1.3×10^{-12}
Fe-15Cr-0.5Cr-0.4C-1Si-1Ni	$\gamma + M_{23}C_6$	Cr_2O_3 scale Carbide dissolution zone	1.4×10^{-12}

Measured oxidation rates and observed reaction morphologies (Table 5.4) fell into two classes. Either a protective chromium-rich oxide scale developed in association with sub-surface alloy carbide dissolution, or a fast-growing iron-oxide scale engulfed the carbide phase. Whereas the ferritic materials always formed protective chromia scales, the austenitic alloys formed non-protective, rapidly growing iron-oxide scales except in the case of the austenite containing silicon. The discussion will return to this observation after consideration of the alloy diffusion processes.

Carbide dissolution depths were measured metallographically and chromium concentrations by electron probe microanalysis, leading to the results shown in Table 5.5. Values for k_c were calculated from the weight gain kinetics

TABLE 5.5 Calculated D_{Cr} Values for Cr_2O_3 -forming Alloys at 850°C

Alloy	Matrix	$X_d/\mu\text{m}$	N_{Cr}^i	$D_{\text{Cr}}/\text{cm}^2 \text{s}^{-1}$
Fe-15Cr-0.5C (forged)	γ	35	0.06	6×10^{-12}
Fe-15Cr-0.5C-1.0Si	α	22	0.10	4×10^{-11}
Fe-15Cr-0.4C-1.0Si-Ni	γ	25	0.10	1×10^{-11}
Fe-15Cr-0.5C-3.0Mo	α	45	0.07	4×10^{-11}

using measured scale compositions. Values for D_{Cr} were then calculated from Eq. [5.91], leading to the results shown in Table 5.5. Examination of these values reveals that D_{Cr} calculated for ferritic alloys are of the order of those reported in the literature. Chromium diffusion in austenitic alloys was slower, as expected, but not as slow as independently measured diffusion coefficients would suggest. Subsequent use of high-temperature XRD to identify the surface phase constitution of reacted alloys confirmed that decarburisation of this region had transformed it from austenite to ferrite. Whether the alloy was ferritic to begin with, or was converted to ferrite in its subsurface zone, the relatively rapid lattice diffusion of chromium to the alloy surface sustained a protective Cr_2O_3 scale.

The effect of silicon on the oxidation behaviour of cast Fe-Cr-C was very strong. Adding 1% to the base alloy made it ferritic and led to growth of a protective Cr_2O_3 scale. Even with an austenitic matrix, which resulted from the further addition of nickel, the silicon-bearing alloy developed a Cr_2O_3 scale. It was concluded that the effect of silicon on oxidation was related not to the change it produced in alloy diffusion, but rather its ability to alter the scale-alloy interface.

The effect of carbide size was important to the reaction morphology [110,112]. Whereas the base alloy Fe-15Cr-0.5C developed a thick iron-oxide scale when reacted in its cast and annealed form, the same alloy formed a protective Cr_2O_3 scale after hot forging (Fig. 5.33). The value of k_p in this latter case was $6.8 \times 10^{-12} \text{ g}^2 \text{ cm}^{-4} \text{ s}^{-1}$. The volume fraction of chromium-rich carbide was the same in both alloy forms, but the precipitates were much smaller (around 1 μm) in the forged material than the 3–5 μm interdendritic carbides typical of the cast alloys. Thus precipitate size, as well as volume fraction, is important in achieving delivery of scale-forming metal to the alloy surface.

In the literature on multiphase alloy oxidation, frequent reference is made to the 1974 study performed by El Dahshan et al. [113] on Co-Cr-C alloys. This work was the basis of the subsequent suggestion [114] of using a minority alloy phase as a ‘reservoir’ of scale-forming metal. Additions of up to 2 wt.% carbon to Co-25Cr caused precipitation of large quantities of chromium-rich carbide and consequently lower chromium content in the metal matrix of these alloys. Nonetheless, the alloys oxidised protectively at 1000°C in pure oxygen. The formation of a protective chromium-rich oxide scale was accompanied by dissolution of the chromium-rich carbides within a shallow alloy subsurface region. It was therefore concluded that localisation of much of the alloy chromium content into precipitates had no effect on oxidation performance, as rapid carbide dissolution yielded the chromium required to form the protective scale.

Viewed in the light of the findings for Fe-Cr-C alloys discussed above, the conclusions reached by El Dahshan et al. are surprising. Their cast, cobalt-base

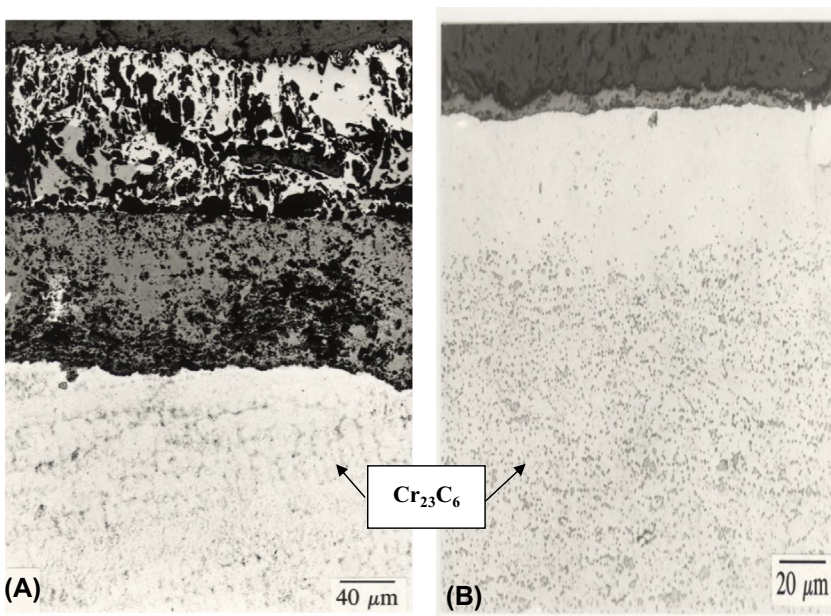


FIGURE 5.33 Oxide scales grown at 850°C on γ -Fe-15Cr-0.5C (A) as cast or (B) forged, demonstrating the effect of carbide size on chromium release [110]. With kind permission from Springer Science and Business Media.

alloys had coarse carbides which would be expected to dissolve slowly. Furthermore, the austenitic alloys might not provide the rapid diffusion required to sustain Cr_2O_3 growth on a Co-Cr alloy.

A re-examination [115] of Co-25Cr-C oxidation at 1000°C has demonstrated that their protective behaviour was in fact due to the presence of silicon contamination, as suggested by Jones and Stringer [116]. Silicon was incorporated into the alloys during annealing in evacuated SiO_2 ampoules. The silicon was thought to promote rapid chromia formation through a surface nucleation effect.

5.8.4 New Phase Formation

The example of copper hot shortness was described in Section 5.1. Accumulation of a layer of copper-rich phase results from noble metal rejection at the scale-alloy interface, just as in the Pt-Ni case investigated by Wagner [12], coupled in this case with a limited solubility for copper in iron. The concentration profile for copper in the reacting system is represented schematically in Fig. 5.34, where the steel is represented as a binary Fe-Cu alloy, and the solubility of copper in FeO is set at zero. At low temperatures, diffusion in

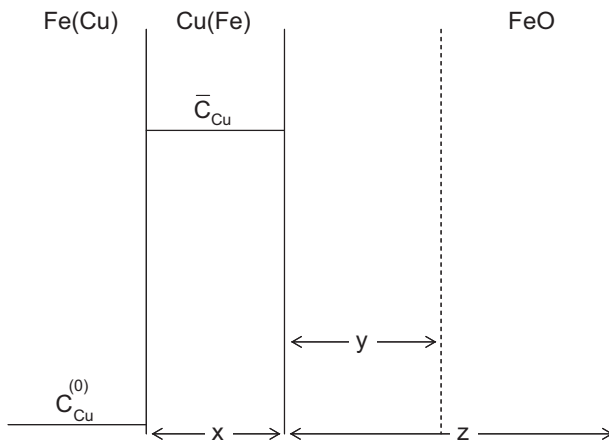


FIGURE 5.34 Schematic concentration profile for copper in oxidised copper-bearing steel, neglecting diffusion into substrate. *Dashed line* shows location of original alloy interface.

the alloy can be neglected, and the thickness of the copper-rich layer can be estimated from a simple mass balance:

$$yC_{\text{Cu}}^{(o)} = x(\bar{C}_{\text{Cu}} - C_{\text{Cu}}^{(o)}) \quad [5.94]$$

where \bar{C}_{Cu} is the average copper concentration in the copper-rich layer and the distances x, y are defined in Fig. 5.34. Combination with Eq. [5.36] then leads to

$$x = \frac{C_{\text{Cu}}^{(o)}}{(\bar{C}_{\text{Cu}} - C_{\text{Cu}}^{(o)})} \frac{V_{\text{FeCu}}}{V_{\text{FeO}}} z \quad [5.95]$$

where the scale is approximated as being entirely wüstite. Under steady-state conditions of parabolic scale growth, the copper layer also thickens according to parabolic kinetics. If V_{FeCu} is approximated as V_{Fe} and \bar{C}_{Cu} estimated from the Fe-Cu phase diagram, then for a 0.47 wt% copper steel, we calculate $x = 2.83 \times 10^{-3}z$. Measured [117] rates of copper layer accumulation were found to be in agreement with values predicted from scaling rates at 1150°C, using the above mass balance. However, measured copper layer thicknesses were less than predicted at 1250°C, particularly in the early stages. This occurred because diffusion of copper into the substrate steel cannot be neglected at high temperatures, as seen in the measured concentration profile in Fig. 5.4.

Another example of new phase formation is provided by the technically important alloys based on γ -TiAl. These have an attractive combination of high temperature strength and low density, but their high temperature

oxidation performance needs improvement. Initial selective oxidation of aluminium leads to formation of the z-phase (approximately $\text{Ti}_{50}\text{Al}_{30}\text{O}_{20}$) as a layer at the alloy surface [118,119]. Examination of the diffusion path in Fig. 5.35 shows that little titanium diffusion is involved, but inward oxygen

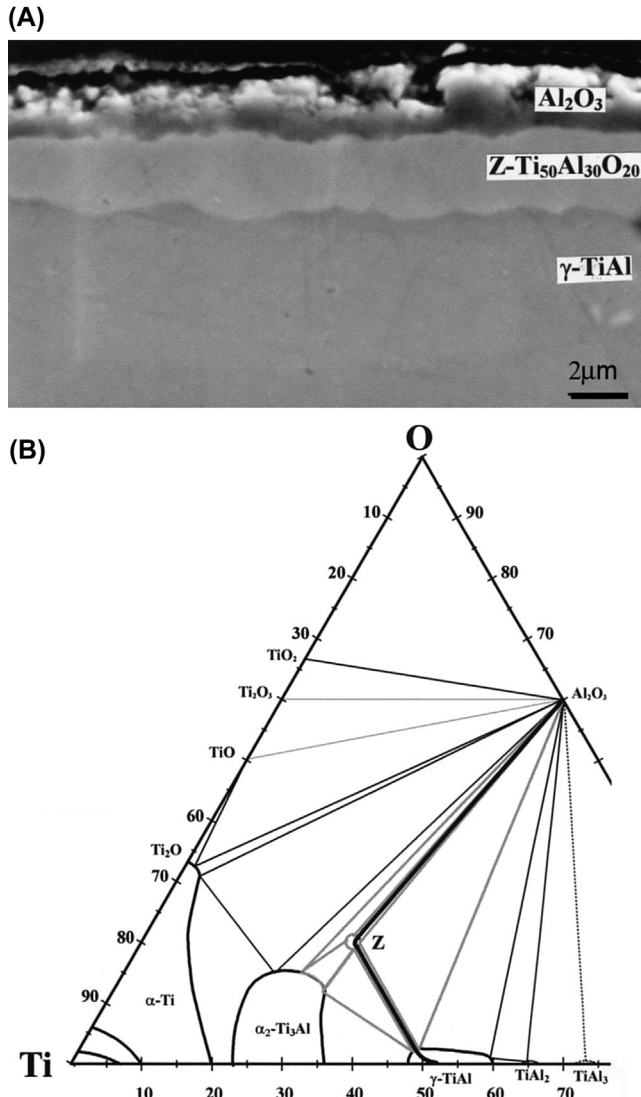
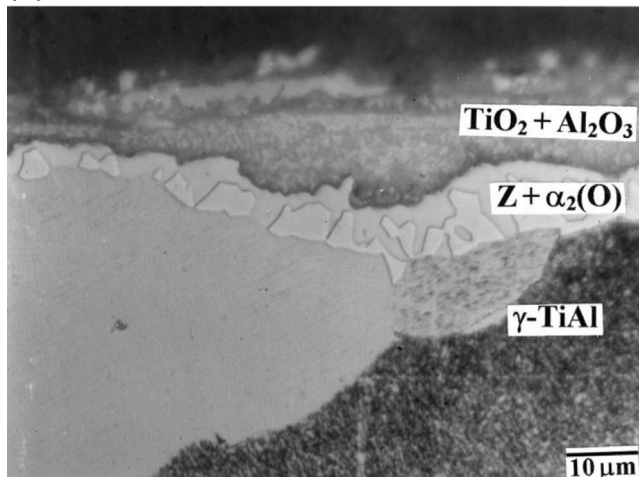


FIGURE 5.35 Oxidation of $\gamma\text{-TiAl}$ at $T = 1000^\circ\text{C}$: (A and B) initial protective behaviour and (C and D) after α_2 precipitation at $\gamma\text{-Z}$ interface. Reprinted from E.H. Copland, B. Gleeson, D.J. Young, *Acta Mater.* 47 (1999) 2937, with permission from Elsevier.

(C)



(D)

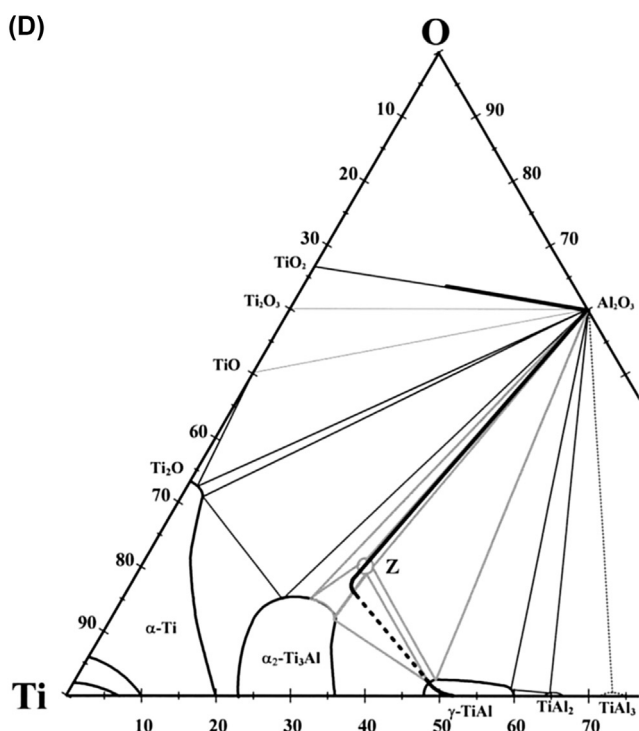


FIGURE 5.35 cont'd

diffusion through the z -phase matches the outward aluminium diffusion. This steady state is not maintained with continued oxidation. Instead, slow aluminium diffusion in the parent γ -phase toward the Z/γ interface leads to its local depletion, morphological breakdown of the interface and ultimately precipitation of oxygen-rich α_2 , as shown in Fig. 5.35. The accompanying volume change leads to cracking of both the z -layer and Al_2O_3 scale, followed by TiO_2 formation and loss of protective behaviour.

5.8.5 Other Transformations

Alloys of three or more components are obviously capable of a greater diversity of phase changes than the relatively straightforward binaries considered so far. An example of practical importance is the Ni-Cr-Al systems, which forms the basis of a number of heat-resisting alloys and coatings. An isothermal section at 1150°C of the phase diagram for this system is shown in Fig. 5.36 [120]. Isothermal oxidation of three-phase (α -Cr + β -NiAl + γ -Ni) alloys led to selective aluminium removal from the alloy and development of a transformed subsurface region [121], as shown in Fig. 5.36. The phases present were identified by electron probe microanalysis: the bright white phase is α -Cr, the mid-grey phase β -NiAl and the light grey one γ -Ni.

As seen from the schematic diffusion path in Fig. 5.36, depletion of aluminium from the three-phase alloys must lead eventually to single γ -phase formation. Dissolution of the β -phase is immediately understandable in terms of the large gradient in aluminium activity developed by the selective oxidation process. Dissolution of α -Cr, on the other hand, was driven by smaller, local gradients in a_{Cr} , resulting from the increased solubility for chromium in γ -Ni developed as the aluminium concentration decreased. For this reason an alloy with a large $N_{\text{Cr}}^{(o)}$ value formed a subsurface $\gamma + \alpha$ region whereas a lower chromium alloy formed single-phase γ -Ni.

5.9 BREAKDOWN OF STEADY-STATE SCALE

When a protective scale of slow-growing oxide can no longer be maintained, other alloy components start to oxidise and alloy consumption is accelerated. This phenomenon of breakdown or breakaway oxidation becomes inevitable when the interfacial concentration $N_{B,i}$ decreases to a value lower than the minimum necessary to maintain the exclusive growth of the desired BO_v scale. It may become possible at higher values of $N_{B,i}$, which are adequate to maintain growth but insufficient to reform a new scale if the existing one is damaged or removed. Although there is no satisfactory way of predicting the latter value, it can be measured experimentally. The problem then becomes one of predicting when the capacity of the alloy to supply B to the interface is exhausted. Similar considerations apply in the case of a scale with some solubility for a second alloy component. Taking

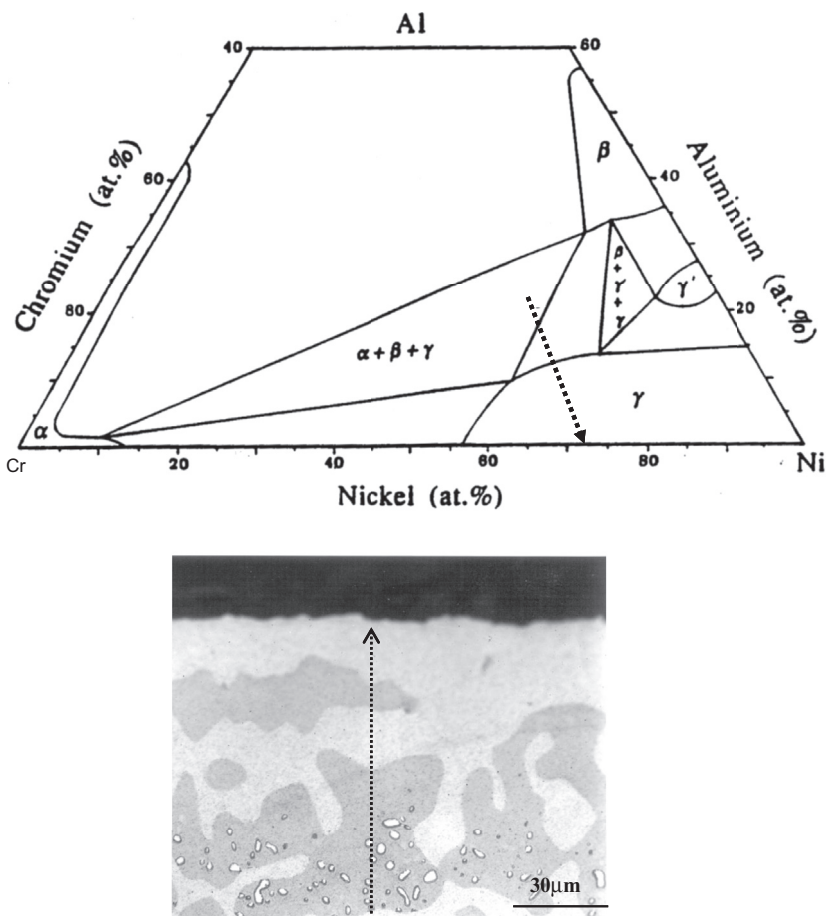


FIGURE 5.36 Isothermal section at 1150°C of Ni-Cr-Al phase diagram [121] and metallographic section of oxidised alloy, showing diffusion path for selective Al₂O₃ formation on three-phase alloy.

the example of an Fe-Cr alloy, it is clear that as $N_{\text{Cr},i}$ decreases, $N_{\text{Fe},i}$ increases and the iron content of the scale also rises. If in the oxide $D_{\text{Fe}}/D_{\text{Cr}} > 1$, iron is increasingly enriched towards the scale-gas interface until an iron rich oxide precipitates.

The ability of an alloy to supply the desired metal to its surface obviously varies with $N_B^{(o)}$, \tilde{D}_{AB} and t , along with the total amount of B in the alloy specimen. Assuming the specimen to be a large, thin sheet so that edge effects can be neglected, the problem is one of diffusion in a single dimension, normal to the oxidising surfaces. We consider first the situation where scale growth is very slow, but alloy diffusion rapid, as will be the case with ferritic alumina

formers. In this event, the N_{Al} profile in the alloy will be almost flat, and the value of $N_{\text{Al},i}$ is equal to the average value \bar{N}_{Al} remaining after aluminium is withdrawn from the alloy into the scale. Clearly, the change in \bar{N}_{Al} with time is significant only if the sheet is extremely thin. This is, in fact, a situation of practical interest because thin sheet material is used in some heat exchangers and as catalyst supports.

This problem has been treated by Quadakkers and Bongartz [122] on the basis that the small movement of the scale-alloy interface can be ignored. The materials examined were Fe-20Cr-5Al and oxide dispersion strengthened (ODS) versions of this and similar alloys. Their oxidation weight gain kinetics are not strictly parabolic [123], obeying instead a power law

$$\Delta W/A = kt^{\frac{1}{n}} \quad [5.96]$$

where $n \approx 3$. The approximately cubic rate law results from the fact that mass transfer in the scale is predominantly via grain boundary diffusion, and the density of grain boundaries changes with time [124] (see Section 3.9). The corresponding amount of aluminium withdrawn from each side of the sheet is

$$\Delta W_{\text{Al}}/A = 1.125kt^{\frac{1}{n}} \quad [5.97]$$

where the dimensionless numerical factor is the Al/O weight ratio in Al_2O_3 . Setting the alloy sheet thickness at $2l$, we find for the reduction in alloy aluminium content, ΔC_{Al} (mole/volume)

$$C_{\text{Al}}^{(o)} - \bar{C}_{\text{Al}} = \Delta C_{\text{Al}} = \frac{1.125kt^{\frac{1}{n}}}{27l} \quad [5.98]$$

with 27 as the atomic weight of aluminium. If the critical value for breakaway is \bar{C}_{Crit} , the time taken to reach it, t_B , is therefore

$$t_B = \left(\frac{27l}{1.125} \frac{C_{\text{Al}}^{(o)} - \bar{C}_{\text{Crit}}}{k} \right)^n \quad [5.99]$$

Quadakkers and Bongartz [122] examined sheets of several ferritic alumina formers oxidised at 1200°C and verified that the concentration profiles of aluminium were essentially flat. Using a critical aluminium level of 1.3 wt% for the breakdown of the alloy MA956, they predicted from Eq. [5.99] the times for breakdown of different sheet thicknesses, shown in Fig. 5.37 as the line labelled ‘no spalling’. Agreement is seen to be good, as would be expected of a simple mass balance.

At greater sheet thicknesses, and longer lifetime, the times to failure are seen to be shorter than predicted. This was attributed to repeated scale cracking and spallation, which occurred at regular intervals. After each of

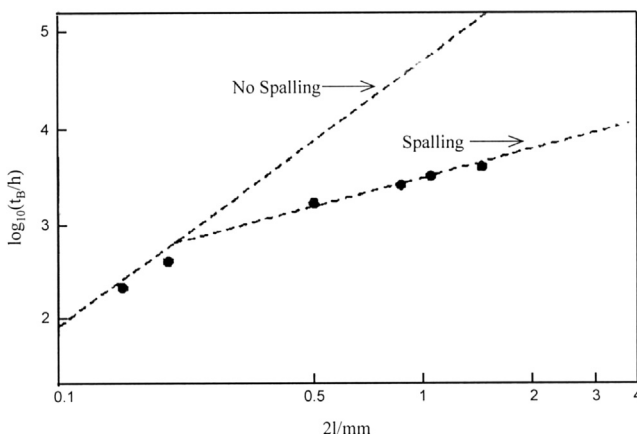


FIGURE 5.37 Lifetime limits for breakdown of Al_2O_3 scales on MA956 sheet. Straight lines predicted from Eqs [5.99] and [5.101], and points observed experimentally [122]. Published with permission from Wiley-VCH.

these events, alumina grew again, according to the same kinetics until the scale next spalled. Assuming equal amounts of aluminium are lost in each spallation event,

$$\Delta W^*/A = 1.125k(t^*)^{\frac{1}{n}} \quad [5.100]$$

where t^* is the time between spallation events and ΔW^* the corresponding aluminium loss, then

$$t_B = \frac{27l}{1.125} \frac{\left(C_{\text{Al}}^{(o)} - C_{\text{Crit}}\right)}{k^n} \left(\frac{\Delta W^*}{A}\right)^{n-1} \quad [5.101]$$

The dashed line in Fig. 5.37 shows behaviour times calculated from Eq. [5.101] on the basis of the observed average $\Delta W^*/A = 2 \text{ mg cm}^{-2}$. Again the simple mass balance prediction is seen to be successful. The more difficult question of predicting when scale spallation will occur is deferred to Chapter 13.

Diffusion in austenitic alloys is significantly slower, and the above description does not apply. Instead, the diffusion profile inside the alloy must be found by solving the general diffusion Eq. [5.12]. Because the interface concentration $N_{B,i}$ becomes a function of time as breakdown is approached, no analytical solution is available. However, a simpler approach is to assume that the surface concentration remains constant until the depleted zones on the two sides of the sheet meet in the middle. At that stage, the surface concentration starts to decrease and breakdown follows.

For diffusion out of a thin, plane sheet $-l < x < l$ in which the concentration is initially $C_B^{(o)}$ and the interfacial concentration is fixed at $C_{B,i}$, the solution is quoted by Crank [125] as

$$\frac{C_B - C_{B,i}}{C_B^{(o)} - C_{B,i}} = \frac{4}{\pi} \sum_{n=0}^{\infty} \frac{(-1)^n}{2n+1} \exp\left(-D(2n+1)^2\pi^2 t / 4l^2\right) \cos \frac{(2n+1)\pi x}{2l} \quad [5.102]$$

for fixed interfaces. As shown by Carslaw and Jaeger [126], diffusion depletion reaches the middle of the sheet when

$$Dt/l^2 \approx 0.05 \quad [5.103]$$

The subsequent decrease in $C_{B,i}$ with time has been treated approximately by Whittle [127,128] on the assumption that $N_{B,i} \ll 1$. Whittle's solution was

$$N_{B,i} = N_B^{(o)} - \left(\frac{\pi k_c}{2D_{AB}}\right)^{\frac{1}{2}} \sum_{n=0}^{\infty} \left[\operatorname{erfc} \frac{nl}{(D_{AB}t)^{\frac{1}{2}}} + \operatorname{erfc} \frac{(n+1)l}{(D_{AB}t)^{\frac{1}{2}}} \right] \quad [5.104]$$

For the specific example of Ni-20Cr oxidised at 1200°C, with $\tilde{D}_{AB} = 2 \times 10^{-10} \text{ cm}^{-2} \text{ s}^{-1}$, $k_c = 2 \times 10^{-8} \text{ cm}^2 \text{ s}^{-1}$ and $2l = 0.25 \text{ mm}$, he calculated $N_{\text{Cr},i} = f(t)$. If the critical interface concentration necessary to prevent spinel formation is $N_{\text{Cr}} = 0.03$, then a breakdown time of $6 \times 10^5 \text{ s}$ would be predicted. This compares with a value of only $2 \times 10^5 \text{ s}$ predicted from Eq. [5.103] for the time at which depletion reaches the sample centre. Clearly, the sheet has a substantial remaining life expectancy, beyond the time defined by Eq. [5.103]. This is confirmed by the results of Douglass and Armijo [129], who showed that NiCr_2O_4 had started to form beneath the chromia scale on this alloy in less than 444 h at 1200°C. It is necessary, therefore, to consider the way in which $N_{B,i}$ decreases after the depletion zones meet in the middle of the sheet.

Whittle's solution Eq. [5.104] provides a reliable method of doing this. The value of the time to occurrence of breakaway oxidation, t_B , can then be estimated if the critical interface concentration, $N_{i,\text{crit}}$, required for continued scale growth is known. Experimentally measured values of this quantity are available in a few instances, and the success of Eq. [5.104] in predicting t_B from $N_{i,\text{crit}}$, k_c and D_{AB} has recently been demonstrated [130]. Moreover, Evans and Donaldson [131] have demonstrated that the approximate solution Eq. [5.104] for diffusion out of a thin plane sheet describes the remnant chromium profile reasonably well.

5.9.1 An Approximate Treatment of Depletion

Whilst Eq. [5.104] is readily evaluated numerically, it lacks transparency and is unsuited to semiquantitative evaluation purposes such as predicting the

temperature sensitivity of t_B . For this reason a more practically useful approximate treatment is of value. Numerical solutions of Eq. [5.104] have been used to explore the way in which t_B varies with the parameters of interest ($l, k_c, D_{AB}, N_0, N_{i,\text{crit}}$), leading to the result [130]:

$$t_B = l^2 \left[\frac{(N_0 - N_{i,\text{crit}})^2}{2k_c} - \frac{\alpha}{D_{AB}} \right] \quad [5.105]$$

where α is a dimensionless constant with a value of 0.37, independent of the alloy system concerned. This expression yields predictions for t_B in close agreement with those of Eq. [5.104] over a wide range of behaviour.

The form of Eq. [5.105] can be understood in terms of alloy diffusion. If D_{AB} is very high, the second term of the right-hand side can be ignored. The first term thus provides an estimate of the maximum lifetime possible, on the basis that diffusion in the sheet is extremely rapid, maintaining the scale-alloy interface concentration at maximum level. This term corresponds to Eq. [5.99] for an alumina former, with appropriate changes in units. The second term provides a correction to the estimate of t_B , accounting for the fact that a diffusion profile develops within the sheet. The gradient of that profile decreases with time, ie, with increased extent of depletion, and the ability of the alloy sheet to supply chromium (or aluminium) to its surface is diminished. The value $\alpha = 0.37$ corresponds to a reduction in the concentration of reacting metal at the middle of the sheet to 50% of its original value [126]. Evidently the size of the diffusion effect on lifetime can be equated to the time required to drain solute from the alloy sheet to the point of 50% depletion at its centre.

The above analyses are of at least indicative value for thin alloy sections, where consumption of the scale-forming metal can occur in a reasonable time. For larger sections, the predictions are optimistic. At 1100°C, a 5 mm section of MA956 (Table 5.1) is predicted from Eq. [5.101] to last for more than 10^5 h. At 1000°C (a realistic maximum for a chromia former), a 5 mm section of Ni-20Cr is predicted on the conservative basis of Eq. [5.103] to last for 8×10^7 h. However, the latter estimate is based on the benign assumption that the Cr₂O₃ scale never cracks or spalls. Moreover, as will be described in later chapters, other modes of failure become likely before the alloy is exhausted of chromium.

5.10 OTHER FACTORS AFFECTING SCALE GROWTH

When alloys scale under steady-state conditions, the identity of the oxide in contact with the alloy is determined by the metal composition at this interface. This composition is related to the original alloy composition and can be calculated from Wagner's analysis of diffusion in the alloy and scale, assuming the latter to be a single-phase, continuous layer. The ratio k_c/D_{AB} is found to be critical in determining interfacial concentrations and, therefore,

the minimum original alloy concentration of a component necessary to sustain the exclusive growth of its oxide scale.

Quantitative application of the theory yields limited success because of its sensitivity to error in experimental measurements of k_c and \tilde{D}_{AB} . Although the theory has been extended to cover solid solution scales, the complexity of their solution thermodynamics and diffusion behaviour means that an even larger body of experimental information is required to permit predictions of scale composition and growth rate. Nonetheless, the theory has been verified in a number of cases, and can clearly be relied upon in a qualitative sense. In describing $N_{B,i}$ in terms of k_c and D_{AB} , the theory successfully accounts for differences between ferritic and austenitic alloys and between chromia and alumina scales. It also succeeds in relating the spatial distribution of components within solid solution scales to the relative oxide stabilities and ion mobilities. These successes are of use in interpreting and, to some extent, predicting scale breakdown.

The values used for the alloy diffusion coefficient have been assumed in this chapter to be these characteristic of bulk or lattice diffusion. Whilst this is reasonable at very high temperatures, it will often be an underestimate at low and intermediate temperatures, where other diffusion pathways such as grain boundaries and dislocations can be more important. The surface finish given to an alloy component before placing it into service can affect the density of grain boundaries and dislocations in the subsurface region. Any low temperature mechanical working of the surface, such as machining, grinding, blast cleaning, shot-peening, etc. deforms the subsurface metal, introducing large numbers of dislocations. As the alloy is heated, the deformed metal recrystallises, forming a generally finer grain and sub-grain structure. These subsurface defects will be present during the transient stage of oxidation and will persist for long times at low temperatures. The consequently higher effective alloy diffusion coefficient is obviously of benefit in rapidly achieving and maintaining protective steady-state growth of chromia or alumina. Several experimental studies [8,132–134] have demonstrated the more rapid formation of Cr_2O_3 on cold-worked alloy surfaces.

Diffusion theory allows calculation of the minimum concentration of an alloy component necessary to sustain the exclusive growth of its oxide. However, this concentration may not be sufficient to achieve such a steady state. In the initial, transient oxidation stage of reaction, essentially all alloy components capable of forming oxides do so. The subsequent development of scale morphology then depends on the competition between continued growth of fast diffusing oxides and replacement of less stable oxides by more stable, but slow growing ones at the oxide-alloy interface. Because this morphological evolution is controlled in part by nucleation and solid-solid interfacial processes, it cannot be described by diffusion alone.

The presence of minority components in the alloy can be critical in their effect on the transient reaction. As discussed in [Section 5.6](#), the phase

transformations leading to $\alpha\text{-Al}_2\text{O}_3$ formation can be accelerated by many alloy additions, either by their chemical doping of alumina or by providing isostructural oxides which act as ‘templating’ sites for α -phase nucleation. Similarly, the addition of cerium to Fe-Cr alloys has been shown [135,136] to promote Cr_2O_3 nucleation.

5.10.1 Environmental Effects on Alumina Phase Transformations

The rates at which metastable alumina phases transform to protective $\alpha\text{-Al}_2\text{O}_3$ also depend on the gas atmosphere to which they are exposed. Water vapour effects on $\gamma\text{-Al}_2\text{O}_3$ transformations have long been known, because of their relevance to the performance of alumina-supported industrial catalysts. Deactivation of these catalysts is caused by alumina sintering, which results from phase transformation. The practical importance of the effect can be gauged from the knowledge that γ -alumina catalyst supports with typical surface areas of $100\text{--}200\text{ m}^2\text{ g}^{-1}$ are replaced by α -alumina with a surface area of about $5\text{ m}^2\text{ g}^{-1}$.

Cooke and Haresnape [137] reported that the minimum temperature for the production of α -alumina from the γ -phase was lowered from 1000 to 400°C in the presence of water vapour. Increasing the value of $p_{\text{H}_2\text{O}}$ in $\text{H}_2/\text{H}_2\text{O}$ mixtures increases the rate of $\gamma \rightarrow \alpha$ transformation at 500°C [138] and 950°C [139]. On this basis, water vapour can be expected to strongly affect the transient oxidation behaviour of alumina formers. The evidence, however, is seemingly inconsistent.

Zhou et al. [140] showed that the $\theta \rightarrow \alpha$ transformation during oxidation of NiAl at 950°C was accelerated by the addition of $\text{H}_2\text{O(g)}$ to air, leading to the earlier establishment of slow oxidation kinetics. Oxidation of Fe_3Al at 950°C is slower in air plus 11% water vapour than in dry air as a result of more rapid α -alumina formation in the wet atmosphere [141]. Similar results were obtained [142] with Kanthal A1 at 1000°C , where a slow-growing scale was developed in air plus water vapour compared with typical transient behaviour in dry air, $\gamma\text{-Al}_2\text{O}_3$ being preserved in the latter case. In the case of an iron aluminide coating, even a low-temperature (650°C) pretreatment in steam was enough to change the outcomes of subsequent exposure to dry air at 900°C [143], leading to slower oxidation kinetics and faster formation of α -alumina.

In contrast, several investigators have reported that water vapour either has no effect on the alumina phase transformations or in fact delays $\alpha\text{-Al}_2\text{O}_3$ formation. Several studies [144–147] of the oxidation of Kanthal AF at temperatures of $600\text{--}900^\circ\text{C}$ led to findings of faster oxidation in air plus water vapour than in dry air and delayed transformation to the α -phase, at least at higher temperatures. An aluminide coating on a nickel-base superalloy oxidised faster in wet air than dry at 1100°C , a difference attributed to the

observed delay in the $\theta \rightarrow \alpha$ transformation [148]. The same authors found that Al-slurry-coated Rene N5 exhibited no such effect.

It is likely that interactions between water vapour-derived species in and on the oxide with minority metal components in the scales are responsible for this diversity of results. In the absence of detailed information on the concentrations and locations of different species within the scales, the question remains unresolved.

The presence of sulphur in the environment can also modify the transient oxidation behaviour of alumina formers [149,150]. Single-phase γ' -Ni₃Al base alloys grow alumina scales more slowly in O₂-0.1% SO₂ than in air at 900°C. The scale grown in air was predominantly θ -Al₂O₃, whereas the α -phase predominated in the sulphur-affected scale. Poisoning of the θ -phase surface by sulphur adsorption was suggested to slow the growth of this oxide, allowing time for the $\theta \rightarrow \alpha$ transformation to take place.

Several metals which form very stable oxides (eg, Ce, La, Y, Hf, etc.) are, for this reason, known as ‘reactive elements’. Their addition to chromia and alumina-forming alloys often affects the strength of the scale-alloy interface, the scale microstructure and the mass transfer mechanisms governing scale growth. These effects are discussed in Chapter 7: *Multiphase Scales*.

REFERENCES

- [1] G.J. Tatlock, H.E. Evans (Eds.), Microscopy of Oxidation 6, Proceedings 6th International Conference Microscopy of Oxidation, Mater. High Temp. vol. 22, 2005.
- [2] P. Syeinmetz, I.G. Wright, G. Meier, A. Galerie, B. Pieraggi, R. Podor (Eds.), High Temperature Corrosion and Protection of Materials 6, Proceedings 6th International Symposium, Les Embiez, France, Mater. Sci. Forum, 461–464, Trans. Tech. Publications Ltd., 2004.
- [3] E. Opila, J. Fergus, T. Maruyama, J. Mizusaki, T. Narita, D. Shifler, E. Wuchina (Eds.), High Temperature Corrosion and Materials Chemistry V, Proceedings 5th International Symposium on High Temperature Corrosion and Materials Chemistry, Honolulu, The Electrochemical Society, Inc., Pennington, NJ, 2005.
- [4] G. Lai, High Temperature Corrosion of Engineering Alloys, ASM International, Materials Park, OH, 1990.
- [5] E.T. Stephenson, Met. Trans. A 14A (1983) 343.
- [6] A.D. Dalvi, D.E. Coates, Oxid. Met. 5 (1972) 113.
- [7] G.C. Wood, I.G. Wright, T. Hodgkiss, D.P. Whittle, Werkst. u. Korros 21 (1970) 700.
- [8] G.S. Giggins, F.S. Pettit, Trans. Met. Soc. AIME 245 (1969) 2495–2509.
- [9] P. Kofstad, High Temperature Corrosion, Elsevier, London, 1988.
- [10] J. Croll, G.R. Wallwork, Oxid. Met. 1 (1969) 15.
- [11] N. Birks, G.H. Meier, Introduction to High Temperature Oxidation of Metals, Edward Arnold, London, 1983.
- [12] C. Wagner, J. Electrochem. Soc. 99 (1952) 369.
- [13] O. Kubaschewski, O. von Goldbeck, J. Inst. Metals 76 (1949) 255.
- [14] D.P. Whittle, D.J. Evans, D.B. Scully, G.C. Wood, Acta Met. 15 (1967) 1421.
- [15] F.S. Pettit, Trans. Met. Soc. AIME 239 (1967) 1296.

- [16] J.A. Nesbitt, *J. Electrochem. Soc.* 136 (1989) 1511.
- [17] G.L. Wulf, M.B. McGirr, G.R. Wallwork, *Corros. Sci.* 9 (1969) 739.
- [18] B.D. Bastow, D.P. Whittle, G.C. Wood, *Oxid. Met.* 12 (1978) 413.
- [19] M.J. Bennett, W.J. Quadakkers, *Mater. Sci. Technol.* 10 (1994) 126.
- [20] H.M. Hindam, W.W. Smeltzer, *J. Electrochem. Soc.* 127 (1980) 1622.
- [21] W.W. Smeltzer, H.M. Hindam, F.A. Elrefaeia, in: R.A. Rapp (Ed.), *High Temperature Corrosion*, NACE, Houston, TX, 1983, p. 251.
- [22] H. Al-Badairy, G.J. Tatlock, *Oxid. Met.* 53 (2000) 157.
- [23] C. Wagner, *Corros. Sci.* 9 (1969) 91.
- [24] D.E. Coates, A.D. Dalvi, *Oxid. Met.* 2 (1970) 331.
- [25] A.D. Dalvi, D.E. Coates, *Oxid. Met.* 3 (1971) 204.
- [26] G.C. Wood, J.M. Ferguson, *Nature* 208 (1965) 369.
- [27] G. Zintl, *Z. Physik. Chem.* 48 (1966) 340 (Frankfurt).
- [28] G. Zintl, *Z. Physik. Chem.* 54 (1967) 110 (Frankfurt).
- [29] C. Wagner, cited by Ref. 25.
- [30] P. Mayer, W.W. Smeltzer, *J. Electrochem. Soc.* 119 (1972) 626.
- [31] P.K. Foster, A.J.E. Welch, *Trans. Faraday Soc.* 52 (1956) 1636.
- [32] L. Himmel, R.F. Mehl, C.E. Birchenall, *Trans. AIME* 197 (1953) 827.
- [33] P. Mayer, W.W. Smeltzer, *J. Electrochem. Soc.* 121 (1974) 538.
- [34] P. Mayer, W.W. Smeltzer, *J. Electrochem. Soc.* 123 (1976) 661.
- [35] A.D. Dalvi, W.W. Smeltzer, *J. Electrochem. Soc.* 121 (1974) 386.
- [36] T. Narita, K. Nishida, *Denki Kagaku* 43 (1975) 433.
- [37] J.P. Orchard, D.J. Young, *J. Electrochem. Soc.* 136 (1989) 545.
- [38] D.J. Young, P. Mayer, W.W. Smeltzer, *J. Electrochem. Soc.* 121 (1974) 889.
- [39] D.J. Young, T. Narita, W.W. Smeltzer, *J. Electrochem. Soc.* 127 (1980) 679.
- [40] W.B. Crow, Report ARL-70-0090, Project No. 7021, Office of Aerospace Research, USAF, Wright-Patterson Air Force Base, OH, 1970.
- [41] T. Narita, K. Nishida, W.W. Smeltzer, *J. Electrochem. Soc.* 129 (1982) 209.
- [42] B.D. Bastow, D.P. Whittle, G.C. Wood, *Corros. Sci.* 16 (1976) 57.
- [43] R.H. Condit, R.R. Hobbins, C.E. Birchenall, *Oxid. Met.* 8 (1974) 409.
- [44] B.D. Bastow, G.C. Wood, *J. Electrochem. Soc.* 9 (1975) 473.
- [45] K. Fueki, Y. Oguri, T. Mukaibo, *Bull. Chem. Soc. Jpn.* 41 (1968) 569.
- [46] S.M.K. Klootsman, A.N. Timofiejew, J.S. Trachtenburg, *Fiz. Met. Metalloved.* 16 (1963) 743.
- [47] D. Toulmin, P.B. Barton, *Geochim. Cosmochim. Acta* 28 (1964) 641.
- [48] F. Gesmundo, P. Costello, F. Viani, J. Philibert, *Oxid. Met.* 47 (1997) 91.
- [49] F. Gesmundo, M. Pereira, *Oxid. Met.* 47 (1997) 507.
- [50] J.S. Dunn, *J. Inst. Met.* 46 (1931) 25.
- [51] F.N. Rhines, B.J. Nelson, *Trans. AIME* 156 (1944) 171.
- [52] C. Wagner, *Trans. AIME* 194 (1952) 91.
- [53] R.L. Levin, J.B. Wagner, *J. Electrochem. Soc.* 108 (1961) 954.
- [54] C. Wagner, *J. Electrochem. Soc.* 103 (1956) 627.
- [55] D.P. Whittle, G.C. Wood, *Br. Corros. J.* 3 (1980) 294.
- [56] N.B. Pilling, R.E. Bedworth, *Ind. Eng. Chem.* 17 (1925) 372.
- [57] D.P. Whittle, G.C. Wood, *J. Inst. Metals* 96 (1968) 115.
- [58] W.H. Gitzen, *Alumina as a Ceramic Material*, American Ceramic Society, Inc, Columbus, OH, 1970.
- [59] ICI Ltd Catalyst Handbook, Wolfe Scientific Books, London, 1970.

- [60] N.S. Koslov, M.Ya Lazarev, L.Ya Mostovaya, I.P. Stremok, *J. Kinet. Catal.* 14 (1973) 113.
- [61] P. Burtin, J.-P. Brunelle, M. Pijolet, M. Soustelle, *Appl. Catal.* 34 (1987) 225.
- [62] D.J. Young, P. Udaja, D.L. Trinn, in: B. Delmon, G.F. Froment (Eds.), *Catalyst Deactivation*, Elsevier, Amsterdam, 1980, p. 331.
- [63] B. Pierragi, *Oxid. Met.* 27 (1987) 177.
- [64] G.C. Rybicki, J.L. Smialek, *Oxid. Met.* 31 (1989) 275.
- [65] M.W. Brumm, H.J. Grabke, *Corros. Sci.* 33 (1992) 1677.
- [66] K. Wefers, C. Misra, *Oxides and Hydroxides of Alumiunium*, Alcoa Technical Paper No. 19, 1987.
- [67] V. Jayaram, C.G. Levi, *Acta Met.* 37 (1989) 569.
- [68] J.K. Doychak, J.L. Smialek, T.E. Mitchell, in: *Int. Congress Met. Corros.*, vol. 1, National Research Council of Canada, Ottawa, 1984, p. 35.
- [69] J. Doychak, J.L. Smialek, T.E. Mitchell, *Met. Trans. A* 20A (1989) 499.
- [70] R. Kartono, D.J. Young, in: E. Opila, J. Fergus, T. Maruyama, J. Mizusaki, T. Narita, D. Schiffer, E. Wachima (Eds.), *High. Temp. Corr. Mater. Chem. V*, The Electrochemical Society, Inc., Pennington, NJ, 2005, p. 43.
- [71] J.L. Smialek, R. Gibala, *Met. Trans. A* 14A (1983) 2143.
- [72] P.Y. Hou, A.B. Paulikas, B.W. Veal, *Mater. High. Temp.* 22 (2005) 535.
- [73] B.A. Pint, L.W. Hobbs, *J. Electrochem. Soc.* 141 (1994) 2443.
- [74] B.A. Pint, J.R. Martin, L.W. Hobbs, *Solid State Ionics* 78 (1995) 99.
- [75] B.A. Pint, M. Treska, L.W. Hobbs, *Oxid. Met.* 47 (1997) 1.
- [76] R. Klumpes, C.H.M. Maree, E. Schramm, J.H.W. de Wit, *Mater. Corros.* 47 (1996) 619.
- [77] E. N'Dah, A. Galerie, Y. Wouters, D. Goossens, D. Naumenko, V. Kochubey, W.J. Quadakkers, *Mater. Corros.* 56 (2005) 843.
- [78] M.J. Bennett, R. Newton, J.R. Nicholls, H. Al-Badiry, G.L. Tatlock, *Mater. Sci. For.* 461–464 (2004) 463.
- [79] R. Prescott, M.J. Graham, *Oxid. Met.* 38 (1992) 233.
- [80] J.R. Nicholls, M.J. Bennett, R. Newton, *Mater. High Temp.* 22 (2003) 429.
- [81] F. Liu, H. Josefsson, J.-E. Svensson, L.-G. Johansson, M. Halvarsson, in: G.L. Tatlock, H.E. Evans (Eds.), *Microscopy of Oxidation 6*, Science Reviews, 2005, p. 359.
- [82] M.C. Maris-Sida, G.H. Meier, F.S. Pettit, *Met. Mater. Trans. A* 34A (2003) 2609.
- [83] W.M. Pragnell, H.E. Evans, D. Naumenko, W.J. Quadakkers, in: G.L. Tatlock, H.E. Evans (Eds.), *Microscopy of Oxidation 6*, Science Reviews, 2005, p. 399.
- [84] R. Cueff, H. Buscail, E. Caudron, C. Issartel, M. Soustelle, *Appl. Catal.* 34 (1987) 222.
- [85] K.M.N. Prasanna, A.S. Khanna, R. Chandra, W.J. Quadakkers, *Oxid. Met.* 46 (1996) 465.
- [86] W. Fei, S.C. Kuiri, S. Seal, *Oxid. Met.* 62 (2004) 29.
- [87] C. Lang, M. Schutze, in: S.B. Newcomb, J.A. Little (Eds.), *Microscopy of Oxidation 3*, Institute of Materials, London, 1997, p. 265.
- [88] A. Andoh, S. Taniguchi, T. Shibata, *Mater. Sci. Forum* 369–372 (2001) 301.
- [89] R. Hales, A.C. Hill, *Corros. Sci.* 12 (1972) 843.
- [90] G.B. Gibbs, R. Hales, *Corros. Sci.* 17 (1977) 487.
- [91] J. Stringer, *Corros. Sci.* 10 (1970) 513.
- [92] J. Smialek, *Met. Trans. A* 9A (1987) 309.
- [93] R. Hutchings, M.H. Loretto, R.E. Smallman, *Metal Sci.* 1981 (1981) 7.
- [94] J. Doychak, M. Rühle, *Oxid. Met.* 32 (1989) 431.
- [95] H.J. Grabke, D. Wiemer, H. Viehaus, *Appl. Surf. Sci.* 47 (1991) 243.
- [96] M.W. Brumm, H.J. Grabke, *Corros. Sci.* 34 (1993) 547.
- [97] S. Shandar, L.L. Seigle, *Met. Trans. A* 9A (1978) 1467.

- [98] J.D. Kuenzly, D.L. Douglass, *Oxid. Met.* 8 (1974) 139.
- [99] A. Kumar, M. Hasrallah, D.L. Douglass, *Oxid. Met.* 8 (1974) 227.
- [100] E.J. Felten, F.S. Pettit, *Oxid. Met.* 10 (1976) 189.
- [101] Y. Cadoret, M.-P. Bacos, P. Josso, V. Maurice, P. Marcus, S. Zanna, *Mater. Sci. Forum* 461–464 (2004) 247.
- [102] B. Gleeson, W. Wang, S. Hayashi, D. Sordelet, *Mater. Sci. Forum* 461–464 (2004) 213.
- [103] D. Caplan, R.J. Hussey, G.I. Sproule, M.J. Graham, *Oxid. Met.* 14 (1980) 279.
- [104] D.A. Woodford, *Met. Trans. A* 12A (1981) 299.
- [105] R.H. Bricknell, D.A. Woodford, *Acta Met.* 30 (1982) 257.
- [106] C. Wagner, *J. Electrochem. Soc.* 103 (1956) 571.
- [107] D.P. Whittle, D.J. Young, W.W. Smeltzer, *J. Electrochem. Soc.* 123 (1976) 1073.
- [108] P. Carter, B. Gleeson, D.J. Young, *Acta Mater.* 44 (1996) 4033.
- [109] D.J. Young, B. Gleeson, *Corros. Sci.* 44 (2002) 345.
- [110] R.N. Durham, B. Gleeson, D.J. Young, *Oxid. Met.* 50 (1998) 139.
- [111] B. Sandman, B. Jansson, J.O. Andersson, *CALPHAD* 9 (1985) 153.
- [112] L.B. Susanto, D.J. Young, *Mater. Corros.* 57 (2006) 467.
- [113] M.E. El Dahshan, J. Stringer, D.P. Whittle, *Cobalt* 3 (1974) 86.
- [114] J. Stringer, D.P. Whittle, I.G. Wright, V. Nagarajan, M.E. El Dahshan, in: *Proc. 8th Int. Congress Met. Corros., Dechema, Frankfurt, 1981*, p. 655.
- [115] R.N. Durham, B. Gleeson, D.J. Young, *Mater. Corros.* 49 (1999) 855.
- [116] D.E. Jones, J. Stringer, *Oxid. Met.* 9 (1975) 409.
- [117] D. O'Neill, D.J. Young, *CAMP-ISIJ* 16 (2003) 1372–1375.
- [118] F. Dettenwanger, E. Schumann, J. Rakowski, G.H. Meier, M. Ruhle, in: S.B. Newcomb, J.A. Little (Eds.), *Microscopy of Oxidation-3*, Institute of Materials, London, 1997, p. 277.
- [119] E.H. Copland, B. Gleeson, D.J. Young, *Acta Mater.* 47 (1999) 2937.
- [120] S.M. Merchant, M.R. Notis, *Mater. Sci. Eng.* 66 (1984) 47.
- [121] S. Han, D.J. Young, *Mater. Res.* 7 (2004) 11.
- [122] W.J. Quadakkers, K. Bongartz, *Werkst. Korros.* 45 (1994) 232.
- [123] W.J. Quadakkers, *Werkst. Korros.* 41 (1990) 659.
- [124] W.J. Quadakkers, D. Naumenko, E. Wessel, V. Kochubey, L. Singheiser, *Oxid. Met.* 61 (2004) 17.
- [125] J. Crank, *The Mathematics of Diffusion*, Clarendon Press, Oxford, 1956.
- [126] H.S. Carslaw, J.C. Jaeger, *Conduction of heat in solids*, Oxford, 1947.
- [127] D.P. Whittle, *Corros. Sci.* 12 (1972) 869.
- [128] H.C. Cowen, S.J. Webster, *Corrosion of Steels in CO₂*, 1974, p. 349. London.
- [129] D.L. Douglass, J.S. Armijo, *Oxid. Met.* 2 (1970) 207.
- [130] D.J. Young, A. Chyrkin, W.J. Quadakkers, *Oxid. Met.* 77 (2012) 253.
- [131] H.E. Evans, A.T. Donaldson, *Oxid. Met.* 50 (1998) 457.
- [132] T.N. Rhys-Jones, H.J. Grabke, H. Kudielka, *Corros. Sci.* 27 (1987) 49.
- [133] T.N. Rhys-Jones, H.J. Grabke, *Mat. Sci. Technol.* 4 (1988) 446.
- [134] S. Leistikow, *Mater. Chem.* 1 (1976) 189.
- [135] M.J. Bennett, J.A. Desport, P.A. Labun, *Oxid. Met.* 22 (1984) 291.
- [136] S. Leistikow, I. Wolf, H.J. Grabke, *Werkst. Korros.* 38 (1987) 556.
- [137] P.W. Cooke, J.W. Haresnape, *Trans. Faraday Soc.* 43 (1947) 395.
- [138] A. Williams, G.A. Butler, J. Hammonds, *J. Catal.* 24 (1972) 352.
- [139] D.J. Harris, D.J. Young, D.L. Trimm, in: *10th Aust. Chem. Eng. Conf.*, 1982, pp. 175–179.
- [140] Z. Zhou, H. Guo, M. Abbas, S. Gong, *Corros. Sci.* 53 (2011) 2943.

- [141] S. Chevalier, P. Juzon, K. Przybylski, J.-P. Larpin, *Sci. Technol. Adv. Mater.* 10 (2009) 045006.
- [142] H. Buscail, S. Heinze, P.H. Dufour, J.P. Larpin, *Oxid. Met.* 47 (1997) 445.
- [143] A. Aguero, M. Hernandez, A. Santaballa, *Oxid. Met.* 79 (2013) 601.
- [144] F. Liu, H. Josefsson, J.-E. Svensson, M. Halvarsson, L.-G. Johansson, *Mater. High Temp.* 22 (2005) 521.
- [145] G. Gotlind, F. Liu, J.-E. Svensson, M. Halvarsson, L.-G. Johansson, *Oxid. Met.* 67 (2007) 251.
- [146] F. Liu, H. Gotlind, J.-E. Svensson, M. Halvarsson, L.-G. Johansson, *Corros. Sci.* 50 (2008) 2272.
- [147] S. Canovic, J. Engkvist, F. Liu, H. Lai, H. Gotlind, K. Hellstrom, J.-E. Svensson, L.-G. Johansson, M. Halvarsson, *J. Electrochem. Soc.* 157 (2010) C223.
- [148] M. Brossard, B. Bouchard, F. Pedreza, *Mater. Corros.* 65 (2014) 161.
- [149] X. Liu, B. Gleeson, *Oxid. Met.* 80 (2013) 517.
- [150] X. Liu, B. Gleeson, *Mater. High Temp.* 32 (2015) 10.